Review Article

Vimal K. Jain* and Gotluru Kedarnath

Tin chalcogenides – a group of multi utility inorganic materials

https://doi.org/10.1515/revic-2024-0141
Received December 30, 2024; accepted March 20, 2025;
published online April 22, 2025

Abstract: Remarkable and unique properties of main group chalcogenides have been exploited for diverse applications owing to their semiconducting properties with a wide range of band gaps and high absorption coefficients. The scope and horizon of their utility is further expanded by modulating the size to nanometre dimensions as well as the number of layers in 2-D layered materials. A number of these materials, like CdTe, $CuInSe_2$, HgCdTe, In_2S_3, PbTe, Bi_2Te_3, etc., are used in several commercial devices, but either their scarce availability in the earth crust or toxicity limits their large-scale utilization. Tin forms several binary, ternary and quaternary chalcogenides which show desirable semiconducting properties. Different compositions and phases exhibit distinct conductivity (p/n-type) and energy band gaps. The band gap energy varies greatly from narrow-band (~0.2 eV) to wide-band (>2.0 eV) depending on the tin chalcogenide. Benign nature and cost effectiveness of tin makes it the most suitable candidate among main group materials. With the flexible tuning of physical and chemical properties, accomplished through different strategies, versatile applications of tin chalcogenides can be realized. This review highlights recent advances on different facets of tin chalcogenide chemistry with their applications in diverse areas.

Keywords: tin chalcogenides; tin sulfide; ternary materials; quaternary materials; photovoltaic solar cells; photocatalysts

Abbreviations

AACVD	Aerosol assisted chemical vapor deposition
Bz	Benzyl
CVD	Chemical vapor deposition
CZTS	Copper zinc tin sulfide (Cu_2ZnSnS_4)
DDT	1-Dodecane thiol
DSSC	Dye sensitized solar cell
HDA	Hexadecyl amine
LIB	Lithium-ion battery
LPCVD	Low-pressure chemical vapor deposition
NC	Nanocrystal
OA	Oleic acid
ODE	1-Octadecene
OLA	Oleyl amine
PCE	Power conversion efficiency
rGO	Reduced graphene oxide
SSMP	Single source molecular precursor
TOP	Trioctylphosphine
TOPO	Trioctylphosphine oxide

1 Introduction

Metal chalcogenides represent a group of important and versatile family of inorganic materials of great technological and biomedical relevance and find wide ranging applications in optoelectronic devices,[1] thermoelectric devices,[2,3] energy harvesting,[4,5] storage devices,[6] catalysts,[7] electromagnetic interference (EMI) shielding[8–10] and sensing platforms, etc. Different classes of metal chalcogenides, *viz.*, binary (ME, ME_2, M_2E_3 where M = metal and E = S, Se, Te), ternary (*e.g.*, $CuInSe_2$,[11] $CuInTe_2$[8] and quaternary (*e.g.*, Cu_2ZnSnS_4[12]) can readily be identified for these applications. Several of them show semiconducting properties. Their physical, chemical, and electronic properties can be further modified by reducing their crystallite size to nanometre dimensions, thus further expanding the scope and horizon of their utility. Brus has demonstrated in the mid-1980s that the optical and electronic properties of bulk CdS differ markedly in nano regime in a size dependent manner and has been attributed to quantum confinement effects.[13,14] This discovery revolutionized the area of metal chalcogenides in the nano regime.

The discovery of graphene by Geim and Novoselov[15,16] further added a new dimension to metal chalcogenide research, in particular transition metal dichalcogenides (TMDs, ME_2). Like graphite, many TMDs have a layered

***Corresponding author: Vimal K. Jain**, UM-DAE Centre for Excellence in Basic Sciences, University of Mumbai, Kalina Campus, Santacruz (E), Mumbai, 400 098, India, E-mail: jainvk@cbs.ac.in. https://orcid.org/0000-0003-2916-9486
Gotluru Kedarnath, Chemistry Division, Bhabha Atomic Research Centre, Trombay, Mumbai 400 085, India, E-mail: kedar@barc.gov.in

structure.[17,18] Each layer (thickness of 6–7 Å) is composed of three covalently bound atoms (E-M-E) where two chalcogen atoms encapsulate the metal atom.[19,20] Each layer is connected by van der Waals bonds which are slightly longer than graphite (3.4 Å) and vary markedly in different materials. The weak van der Waals forces between the layers can facilitate exfoliation of TMDs into the sheet of single layer. These TMDs exhibit varied electronic properties ranging from insulating, semiconducting, semi-metallic, metallic to superconducting.[21] The unique and remarkable properties of ultrathin layers of TMDs, distinct from their 3-D counterparts, make them potentially interesting candidates for numerous applications.[22–24] Interestingly, several main group chalcogenides, like TMDs, also have layered structures which can be exfoliated.[25] The binary layered main group chalcogenides with formal stoichiometries of ME, ME_2 and M_2E_3 have covalently bonded 2D stacking units of E–M–M–E, E–M–E and E–M–E–M–E atomic layers, respectively.[22] The binding energy of SnS and SnSe layers has been calculated as 30 and 10 meV $Å^{-2}$, respectively making them easily exfoliable materials and by changing the number of layers band gap can be tuned over a large range (0.6 and 0.4 eV for SnS and SnSe, respectively).[26] Depending on the metal-chalcogen coordination environment and stacking order within the individual layers different polymorphic structures differing in symmetries can exist.[27]

The interest in main group metal chalcogenides and also those of zinc triad [for being formed with the filled d^{10} configuration[28]] has expanded due to their possible applications in electronics and energy-related demands which is driven by their adaptable electronic properties, semiconducting behaviour and high thermoelectric performance. A number of them are now used in commercial devices. These include CdTe and $CuInSe_2$ for photovoltaic solar cells,[4,5] HgCdTe (MCT) infrared detectors,[29] In_2S_3 as passivating and buffer material,[30] PbTe, Bi_2Te_3 for thermoelectric devices.[2,31–33] Although several of them are used in commercial devices, most of them are based on elements which are either scarcely available in the earth crust (*e.g.*, In, Te) or toxic (*e.g.*, Cd, Hg, Pb) in nature, thus necessitating for alternate materials with similar properties. Tin, which forms several binary, ternary and quaternary chalcogenides of desirable properties, does not have such limitations and therefore emerges as the most suitable candidate among the main group chalcogenide materials. Furthermore, its cost effectiveness and benign nature gives added advantage to their applications. Accordingly, in this review, different facets of tin chalcogenide chemistry with their applications are presented so as to further accelerate the exploration of tin chalcogenides.

2 Tin chalcogenide crystal structures

Tin forms numerous chalcogenides which can be clubbed into binary, ternary and quaternary compounds depending on the number of constituent elements (Figure 1). These compounds in general exhibit semiconducting properties with direct and/or indirect band structures. Substitution of constituent elements in the binary system has been practiced for engineering the band-gap and band-structures of semiconductor compounds. Both vertical -substitution (substituting an element by another in the same group of the Periodic Table) and cross-substitution, established for fabricating chalcogenide materials,[34–37] have been developed to design several ternary and quaternary tin chalcogenides (Scheme 1).

2.1 Binary tin chalcogenide materials

Binary tin chalcogenides exist in two stoichiometries, *viz.* SnE (E = S, Se, Te) and SnE_2 (E = S or Se) except for Sn_2S_3 which possesses a non-equilibrium phase. In general, binary tin chalcogenides are layered compounds and crystallize into cubic, hexagonal, trigonal and orthorhombic space groups (Table 1). Thermodynamically stable phase of monochalcogenides, α-SnS and α-SnSe, have orthorhombic *Pnma* structure at room temperature. The structure of SnS consists of double layers of tin and sulfur atoms, similar to deformed NaCl structure, where each layer is bonded through weak van der Waals forces. The Sn^{2+} ion adopts a distorted octahedral configuration defined by six sulfur atoms. The distortion can be attributed to the existence of three short

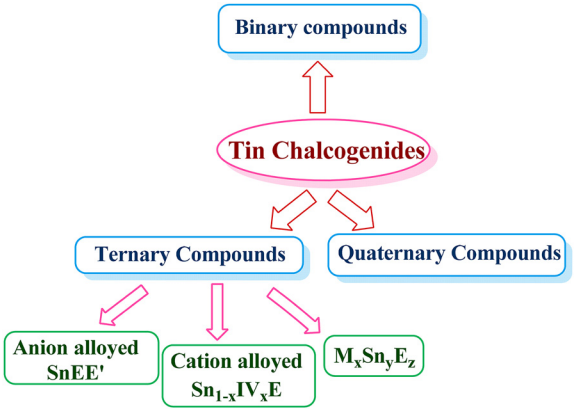

Figure 1: Different types of tin chalcogenides, where '**IV**' is any group IV element other than tin and E = S, Se or Te.

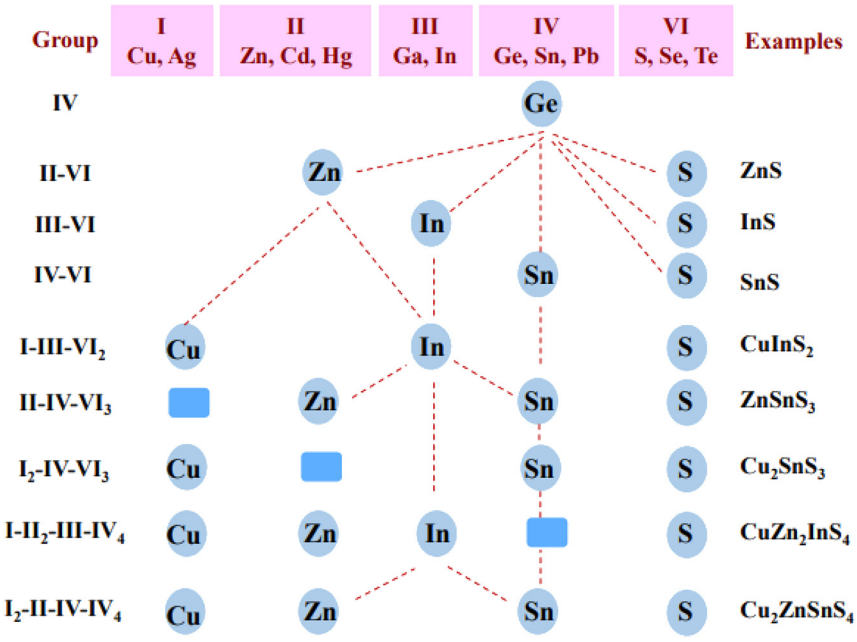

Scheme 1: Cross-substitution of elements in binary chalcogenides to fabricate ternary and quaternary chalcogenide materials.

Table 1: Crystal structures of binary tin chalcogenides.

Sn_xE_y	Crytal system	Space group
α-SnS	Orthorhombic	*Pnma* (62)
β-SnS	Orthorhombic	*Cmcm* (63)
π-SnS	Cubic	$P2_13$ (198); *F*-43*m* (216); *Fm*-3*m* (225)
SnS_2	Hexagonal	$P6_3mc$ (186)
	Trigonal	*P*-3*m*1 (164)
	Cubic	*Fd*-3*m* (227)
Sn_2S_3	Orthorhombic	*Pnma* (62)
α-SnSe	Orthorhombic	*Pnma* (62)
β-SnSe	Orthorhombic	*Cmcm* (63)
π-SnSe	Cubic	*Fm*-3*m* (225); $P2_13$ (198)
$SnSe_2$	Orthorhombic	*Pnma* (62)
	Trigonal	*P*-3*m*1 (164)
α-SnTe	Orthorhombic	*Pnma* (62)
β-SnTe	Cubic	*Fm*-3*m* (225); *F*-43*m* (216); *Pm*-3*m* (221)
γ-SnTe	Orthorhombic	*Pnma* (62)

and three long Sn–S bonds.[38] The orthorhombic structure of SnSe is similar to three-dimensional deformed rock-salt structure in which Sn and Se atoms are part of layered structure. The two planes of Sn–Se chains are zipped through van der Waal interactions. The orthorhombic SnSe unit cell consists of distorted $SnSe_7$ units in which there are three short and four long Sn–Se bonds. The Sn(II) lone pair occupies one of the symmetrical sites and imparts its effect to deform the crystal structure.[39,40] The double layer structure of SnE (E = S or Se) imparts anisotropic properties to these materials.[39] Interestingly, both α-SnS and α-SnSe (orthorhombic, space group *Pnma*) undergo phase transition above 600 °C and at 523 °C, respectively to orthorhombic *Cmcm* (β-SnE) with the shifting of Sn and E along (100) direction.[41,42] The phase transition of SnE (E = S or Se) from α-to β-form has been reported as second order transition of displacement type.[43] In addition to orthorhombic structures, SnS also has a metastable cubic structure,[44] while for SnSe a cubic phase has been identified recently. Different crystallographic structures of SnE are depicted in Figure 2.[45,46]

Under atmospheric conditions, SnTe crystallizes in a cubic structure with space group *Fm*-3*m*. Tin and tellurium atoms occupy the octahedral sites. For the octahedral coordination, each atom should have on an average six valence electrons per atom, but both Sn and Te have only three valence electrons. Because of inadequate number of valence electrons, the various electronic configurations resonate resulting in soft Sn–Te bonding which subsequently interacts with the lone pair of tin to give distorted crystal structure. This phase is stable up to 727 °C but below 100 K rhombohedral phase of SnTe exists.[47,48] However, under pressure the cubic phase of SnTe changes to an orthorhombic structure (γ-SnTe) with *Pnma* space group.

Ground state SnS_2 has the trigonal crystal structure belonging to *P*-3*m*1 space group.[49] The structure comprises edge sharing octahedral SnS_6 units where Sn^{4+} ions are surrounded by six sulfur atoms. The SnS_6 units lie along the *c*-axis. Each unit is connected with each other by weak van der Waals interactions (Figure 3).[45] Similarly, $SnSe_2$ crystallizes in a trigonal system in a *P*-3m1 space group and can also adopt orthorhombic structure.[49] Thermogravimetric analysis of SnS_2 and $SnSe_2$ revealed that both compounds decompose at 570 and 340 °C, respectively to the corresponding tin monochalcogenide (SnE) with the

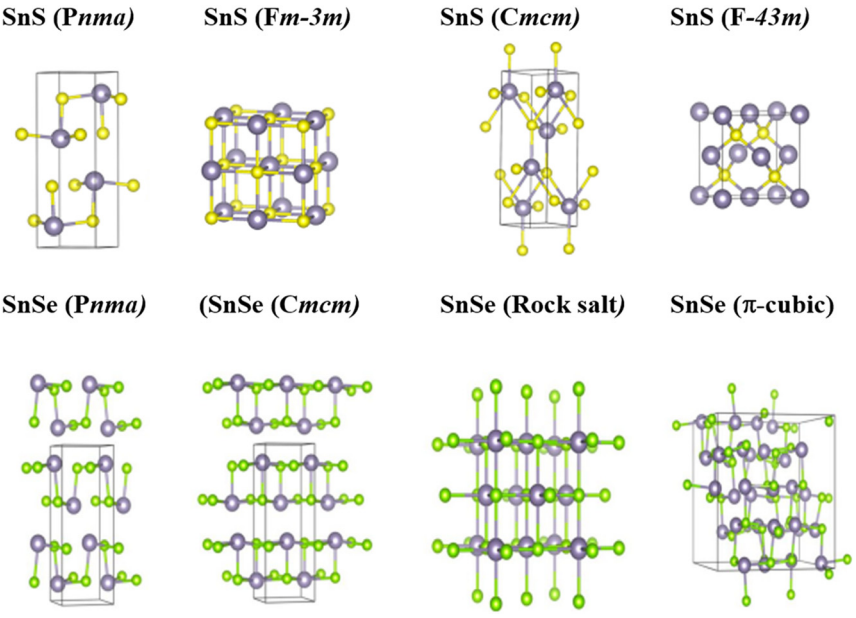

Figure 2: Crystal structures of SnS and SnSe (tin in grey, sulfur in yellow and selenium in green) (reproduced from American Chemical Society[45] and with permission from Royal Society of Chemistry.[46]

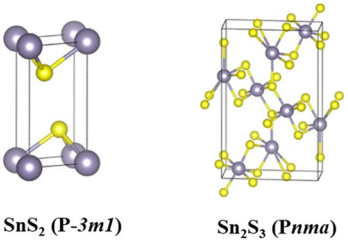

Figure 3: Crystal structures of SnS_2 and Sn_2S_3 (tin in grey and sulfur in yellow) (reproduced from American Chemical Society).[45]

elimination of sulfur/selenium.[50] The Sn_2S_3 is a mixed valent tin chalcogenide. It adopts a ribbon-like structure where the Sn^{2+} and Sn^{4+} ions are surrounded by sulfur atoms in a trigonal bipyramidal and octahedral geometries, respectively. It shows n-type conductivity. Depending on preparative method, band gap energy varies between 0.95 and 2.2 eV.

2.2 Structure related properties of binary tin chalcogenides

Binary tin chalcogenides constitute an important class of 2D layered materials by virtue of its crystallographic structure. These tin chalcogenides have covalent bonding within the planes whilst having interlayer connection through van der Waals forces. Scion of these weak forces results in slices of 2D layered sheets. For instance, orthorhombic SnS and SnSe which has distorted NaCl crystal structure exhibit aforementioned bonding leading to 2D layered materials. Here, lone pair electrons of Sn(II) lodges at one of the symmetrical sites leading to deformed structure which further imparts anisotropic nature to these materials.[39] However, in cubic phase (rock salt and zinc blende structures) of SnS and SnSe, asymmetric bonding dictated by lone pair of Sn^{2+} causes both tin and chalcogen atoms to occupy four discrete crystallographic sites. While SnTe preferably existing in cubic structure get distorted due to interaction of delocalized electron cloud of soft Sn–Te bonding with lone pairs of Sn^{2+}. This results in the formation of 0D materials preferably in case of SnTe materials while SnTe sheets can be produced by growth directing methods like template mediated anion exchange[51] and vapor-liquid-solid-methods,[52] etc.

Like tin monochalcogenides, tin dichalcogenides (SnE_2), also exhibit CdI_2-type layered structure wherein tin and chalcogen are covalently bonded within the layer and inter-layers are held together by van der Waals forces. This type of structure drives the formation of 2D sheets. Furthermore, sesquisulfide i.e. Sn_2S_3 also assumes ribbon like structures. Owing to their layered structure, tin chalcogenides display remarkable properties which make them potential electrode material for energy storage devices. While anisotropic structure, resonant bonding and local structural distortion resulting in anharmonicity and hence lowering of thermal conductivity brand them as good thermoelectric materials. Additionally, suitable band gap and high absorption coefficient for harvesting solar energy combined with effective carrier mobility proffers tin chalcogenides as an efficient active material for photovoltaics,[39,53] and optoelectronics.[39] Features such

as narrow band gap, heavy constituent elements and substantial spin–orbit coupling project them as an important class of topological materials.[54]

2.3 Ternary tin chalcogenide materials

There are several ternary tin chalcogenides, such as Cu_2SnE_3 (E = S or Se), Cu_2SnSe_4, $ZnSnS_3$, etc. In the Cu–Sn–S Gibbs phase triangle, several ternary compounds have been identified which include orthorhombic Cu_4SnS_4, Cu_2SnS_3, orthorhombic or tetragonal Cu_3SnS_4 and more complex structures, Cu_4SnS_4, Cu_4SnS_6, $Cu_4Sn_7S_{16}$ and $Cu_4Sn_{15}S_{32}$, etc.[55,56] These phases are mainly p-type semiconductors except $Cu_4Sn_7S_{16}$ which is an n-type semiconductor,[57] although some metallic phases like orthorhombic Cu_3SnS_4 (a mixed valence compound) and rhombohedral Cu_4SnS_6 are also encountered. Among ternary systems, Cu_2SnE_3 (E = S and Se) have received much attention.[56] These compounds exist in various polymorphic forms like cubic, tetragonal, hexagonal, monoclinic, triclinic, and orthorhombic and can undergo phase transition at different temperatures. For instance, Cu_2SnS_3 at low temperature exists in a tetragonal chalcopyrite structure which can be converted into the metastable zinc blende structure at 780 °C, and wurtzite structure at 856 °C.[55] The formal oxidation states of Cu, Sn and E in Cu_2SnE_3 have been deduced as +1, +4 and −2, respectively from X-ray photoelectron spectroscopy.[58]

2.4 Quaternary tin chalcogenide materials

The quaternary tin chalcogenide compounds, Cu_2MSnE_4 (M = Zn, Cd, Mn, Fe, Co, Ni, etc., E = S or Se) exist in different polymorphs of closely related crystallographic structures.[59–62] In these structures every sulfur anion is bound with four cations ($2Cu^+$, M^{2+} and Sn^{4+}) and *vice versa* and the cations occupy different positions in the closely related structures. Depending on the preparative method, these compounds can crystallize into thermodynamically stable body-centered tetragonal kesterite, stannite and primitive mixed Cu–Au (PMCA) phases[63] and a metastable wurtzite phase (hexagonal)[62] (Figure 4). Besides these structures, wurtzite derived structures, *e.g.*, wurtzite–kesterite and –stannite phases, can also form.[64,59,65] Different CZTS phases can form at different temperatures.[66] The kesterite phase, thermodynamically the most stable structure,[67] can undergo phase transition into disordered kesterite 260 °C, but at much elevated temperatures (866–1,002 °C) can transform into sphalerite phase–a fully disordered cubic structure.[60] Similarly, annealing of metastable wurtzite CZTS nanorods (diameter and length: 9 ± 0.5 and 35 ± 1 nm, respectively) at 400 °C results into kesterite phase within a few seconds.[68] Different phases of CZTS differ only slightly in energy.[69–71] The stannite and PMCA phases are higher in energy by 2.9 and 3.2 meV/atom, respectively than the kesterite phase.[69,71] Because of small differences in total energy values and similar lattice constants, kesterite and stannite structures can often co-exist in the synthesized samples.

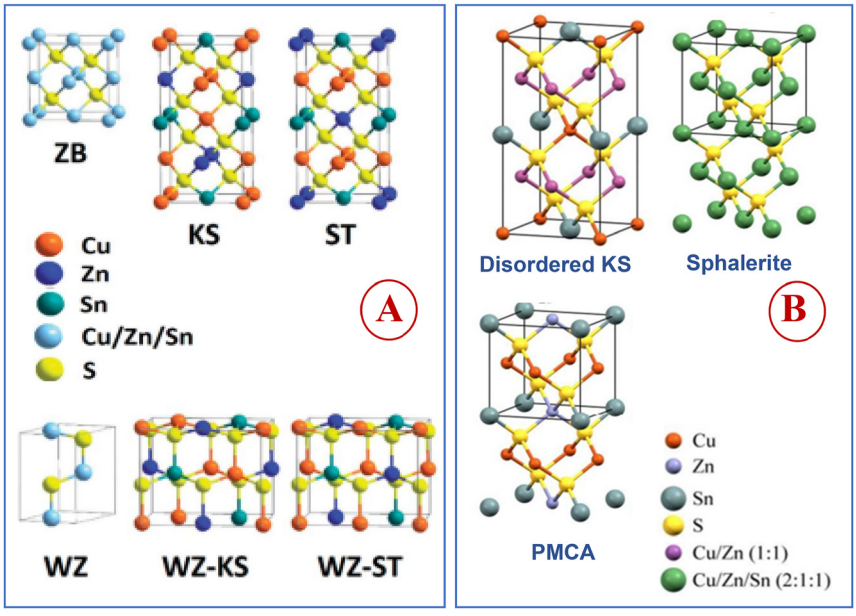

Figure 4: Schematic representation of quaternary Cu_2ZnSnS_4 structures derived from zinc-blende (ZB) and wurtzite (WZ) phases of binary ZnS (KS = kesterite; ST = stannite; (KS), WZ-KS = wurtzite–kesterite; and WZ-ST = wurtzite–stannite) (adapted from Royal Society of Chemistry[64] (A) and with permission from Royal Society of Chemistry[63] (B).

2.5 Band-gap of metal chalcogenides

Tin chalcogenides are semiconductor materials. Different compositions and phases exhibit distinct conductivity (p/n-type) and energy band gaps. The band gap energy varies greatly from narrow-band (~0.2 eV) to wide-band (>2.0 eV) depending on the tin chalcogenide. The band structures and band-gaps can be modulated by altering the size of the material to nano dimension, *i.e.,* as nanoparticles/nanocrystals (NCs) (one of the dimensions in the range of 1–100 nm). The band structure can be modified by reducing one of the dimensions of these particles to smaller than the Bohr exciton radius, as a consequence such particles show quantum confinement effect.[64,72,73] The quantum size effect is manifested in shifting of band gap to higher energy (a blue shift) relative to the band for bulk counterparts (Figure 5). Besides size-effect, physicochemical properties of NCs are also affected by their compositions, morphologies, crystal structures, etc. As several tin chalcogenides have layered structures, they exhibit highly layer-dependent electronic properties.[74–77] For example, the indirect band gap of bulk SnS_2 increases from E_g = 2.18 eV–2.41 eV for the single layer (Table 2).[75–77] The optoelectronic properties of tin chalcogenides, in general for metal chalcogenides, strongly depend on preparative method, size, morphology, phase purity, etc. Due to this reason, the value of band gap energy often differs in different publications. Therefore, selection of a synthesis/deposition of thin film method is of paramount importance for proposed application of the material.

Table 2: Indirect and direct band gaps of bulk and few layers of SnE (E = S or Se)[76,77] and SnE_2 (E = S or Se).[75]

SnE_x (x = 1 or 2)	System	E_g (indirect) (eV)	E_g (direct) (eV)
SnS	Bulk	1.07	1.32
	Two-layer	1.57	1.98
	Single-layer	2.57	2.72
SnSe	Bulk	0.9	1.3
	Two-layer	1.47	1.62
	Single-layer	1.63	1.66
SnTe	Bulk	–	0.18
SnS_2	Bulk	2.18–2.28	2.56–2.88
	Quadra-layer	2.22	2.50
	Tri-layer	2.29	2.54
	Bi-layer	2.34	2.57
	Single-layer	2.41	2.68
$SnSe_2$	Bulk	0.98–1.07	1.28–1.84
	Quadra -layer	1.26	1.58
	Tri-layer	1.37	1.68
	Bi-layer	1.51	1.83
	Single-layer	1.69	2.04

3 Synthesis of metal chalcogenides

Over a period, several synthetic approaches have evolved for the preparation of metal chalcogenides, their nanocrystals, and thin films.[22,78] The traditional solid-state synthesis is carried out by reacting constituent elements in required stoichiometric ratio in sealed tubes at high temperatures (>600 °C) and/or high pressure which often yields coarse and aggregated particles.[79,80] Several synthetic approaches based on solution-phase and gas-phase processes have emerged due to their high versatility and ease. They do not require extreme conditions of traditional solid-state synthesis. Now nano-materials with high composition and phase purity, crystal phases, precise size (monodispersed material), morphologies, doping defects and surface properties required for the desired applications can be produced with greater reproducibility under moderate reaction conditions. Different synthetic methods can be categorized broadly in two groups, viz. top-down or fabrication method and bottom-up or synthesis approach (Scheme 2). Different synthetic methods might yield products exhibiting different characteristics like physical, chemical, electronic, and surface properties.

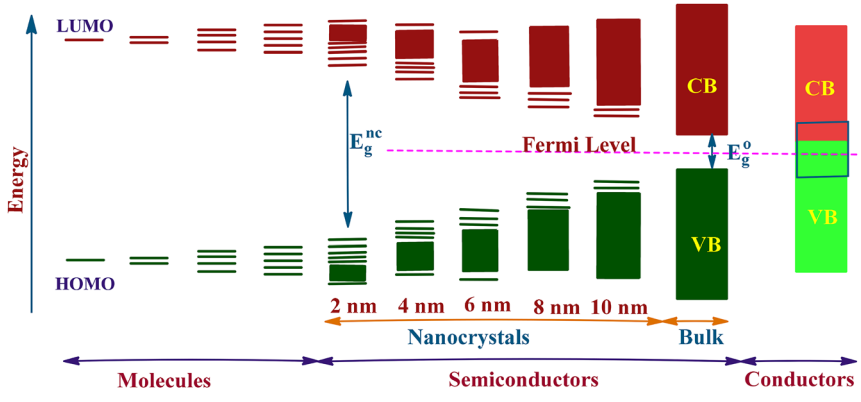

Figure 5: Schematic representation of evolution of energy levels from molecules to semiconductors to conductors. E_g^{nc} and E_g^{o} indicate band energy of nanocrystals and bulk semiconductors.

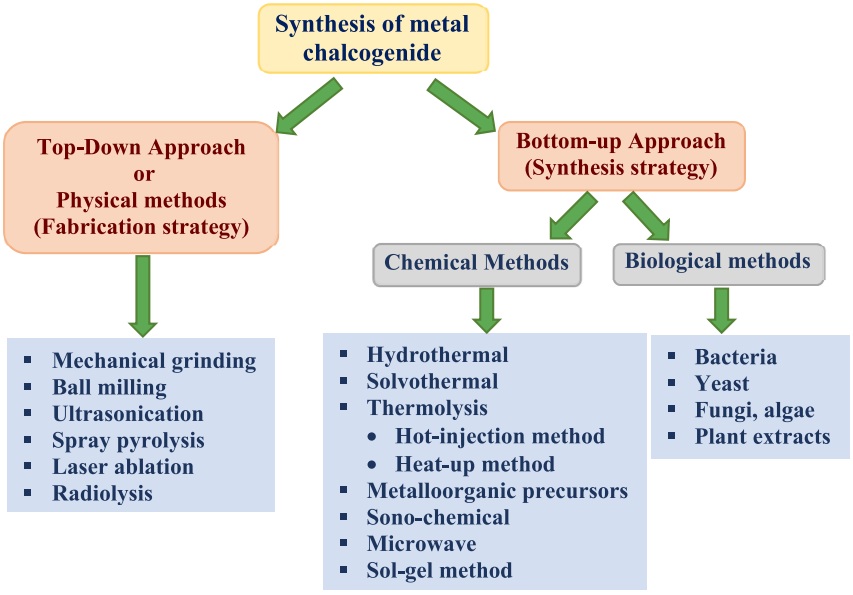

Scheme 2: Different synthetic approaches for metal chalcogenide nanocrystals.

Bottom-up methods are widely employed for the synthesis of tin chalcogenides owing to the control over broad chemical compositions, morphology, dimension, and crystal phases.[64,81–84] These include: hot-injection synthesis,[85] heat-up synthesis,[86] hydrothermal/solvothermal synthesis,[87,88] microwave-assisted processes, polyol methods. In hot injection method a chalcogen precursor containing solution is swiftly added into a hot solution of a metal salt and capping agents, whereas in heat-up method all the reactants (metal precursor, chalcogen precursor, capping agent) are mixed at low temperature in one-pot and subsequently the contents are heated to an appropriate high temperature to trigger the formation of metal chalcogenide.[82,84] In hydrothermal (in water)/solvothermal (in non-aqueous solution) methods reaction between metal compounds and chalcogen source is carried out in a sealed autoclave at higher temperature and pressure to promote the formation of crystals.[22] Quaternary semiconductors are usually prepared by hot-injection and heat-up methods.[81] These protocols involve multi-source precursors of metal and chalcogen, and a variety of other reagents to obtain nanomaterials of required compositions. The tin source is realized by its salts such as $SnCl_2{\cdot}2H_2O$, $Sn(OAc)_2$, $[Sn\{N(SiMe_3)_2\}_2]$, $SnCl_4{\cdot}5H_2O$, $Sn(OAC)_4$, while chalcogen source, E (E = S, Se or Te) is accomplished by Na_2S, thiourea, thioacetamide, thiols (1-dodecane thiol, tert-dodecane thiol) or H_2S in case of S; selenourea or selenols, SeO_2 and Ar_2Se_2 for Se; Ph_2Te_2 for Te. Additionally, elemental chalcogen (S, Se, Te) dissolved in a Lewis base like OLA or TOP or in organic solvents, such as ODE, ethylene glycol has also been employed as a chalcogen source.

The multi-source precursor route has its own merits and limitations. For instance, the dual/multiple source method has an advantage of separation of nucleation and growth stages in a controlled fashion as compared to other methods in thermolysis mode and results in an exceptional control over the crystallite size and shape of nanocrystals. However, multiple source precursors in general are toxic, volatile, hygroscopic and often expensive. For instance, H_2S used as a sulfur source is toxic, $SnCl_4$ is hygroscopic while $[Sn\{N(SiMe_3)_2\}_2]$ is air sensitive posing inconvenience in handling. The formation of various secondary phases including binary metal chalcogenides along with elemental metal or chalcogen further aggravates the synthesis protocol using multiple source precursors. For example, synthesis of SnS nanorods by solvothermal method using $SnCl_2{\cdot}2H_2O$ and Na_2S for LIB anode material, produced the product contaminated with SnS_2.[89] For deposition of high-quality thin films, multiple source precursors may prove unreliable for reasons like pre-gas phase reactions, poor stoichiometric control, and formation of defective films due to high deposition temperatures. Furthermore, when the precursors are highly volatile, they afford non-stoichiometric and impure materials as the precursors may volatilize from the reaction container even before its involvement in the reaction.[90]

To overcome prevalent deficiencies of dual/multi source precursors method, the use of single source molecular precursors, either in heat-up or hot-injection route, has emerged as a remarkable approach for the synthesis of metal chalcogenides. In this approach pre-existing M-E bonds facilitate in yielding uniformly monodispersed nanoparticles.[91–93] Additionally, most of the prudently designed single-source precursors are air-stable, less toxic and are convenient to handle, purify and characterize. The programmed pre-existing bonds in them help in stoichiometric delivery of material through

molecular level mixing. Further, materials with fewer defects can be realized through thoughtful design of SSMPs by judicious selection of ligands to develop precursors which have lower decomposition temperature with cleaner decomposition mechanisms. Additionally, versatility of SSMP is utilized both for the NCs synthesis and for thin films deposition by AACVD technique. Thin films deposition using SSMP in AACVD method is much simpler due to easy precursor delivery and handy processing conditions compared to other conventional CVD method using dual source precursors and eliminates use of toxic, pyrophoric, volatile reagents such as metal alkyl organometallic compounds. SSMP also offers better control over thin film composition and homogeneity due to molecular level premixing of the desired elements in SSMPs.

SSMPs, despite several merits, have their own share of drawbacks such as existence of high nuclearity complexes, tendency to oligomerize which results in decreased solubility in common organic solvents posing difficulty in their purification and characterization. Such complexes usually have high decomposition temperatures compared to monomeric derivatives and can produce several unwanted impurities along with the desirable product due to their incomplete decomposition. The merits of SSMP are also lost if the bonds between the core elements of SSMP are comparable or weaker than those between the core and the organic ligands. Such a SSMP, assumes an unfavourable decomposition path leading to unwanted by-products. For instance, synthesis of SnSe using $(Bz_3Sn)_2Se$ produced samples contaminated with elemental tin.[94] Another significant problem associated with SSMP having bulkier ligands or SSMPs which undergo improper cleavage often yield products contaminated with carbon impurity.

High-quality thin films of metal chalcogenides are required for various applications like solar cells, thermoelectric devices, etc. Several methods have been developed for deposition of metal chalcogenide thin films (Scheme 3).[95] Spray pyrolysis and chemical vapor deposition methods are most commonly employed for deposition of tin chalcogenide films. CVD has been considered as a promising route to grow high-quality tin chalcogenide thin films in a scalable and controllable manner with desired orientation and morphology.[22,93] Owing to the versatility of CVD method, several variants of this technique have been developed in the recent past. These include metal–organic CVD (MOCVD), AACVD, atmospheric pressure CVD (APCVD), low pressure MOCVD (LPMOCVD), etc.

3.1 Synthesis of binary tin chalcogenides

A variety of tin chalcogenolate complexes have been engaged as precursors for binary tin chalcogenide synthesis. Tin complexes in both + 2 and + 4 oxidation states have been used. Complexes of tetravalent tin, at large, have monomeric structures, while tin(II) chalcogenolates of general formula $[Sn(ER)_2]$, adopt several coordination geometries, viz. monomeric (*e.g.*, $[Sn(SC_6H_2Bu^t_3\text{-}2,4,6)_2]$),[96] dimeric (*e.g.*, $[Sn(Sepy)_2]$,[97] $[Sn\{ESi(SiMe_3)_3\}_2]_2$,[98] trimeric (*e.g.*, $[Sn(SC_6H_3Pr^i_2\text{-}2, 6)_2]_3$)[96] and 1-D polymer (*e.g.*, $_\infty{}^1[Sn(SBu^n)_2]$[99]; $_\infty{}^1[Sn(SBu^t)_2]$[100]; $_\infty{}^1[Sn(EPh)_2]$ (E = S, Se, Te).[101]

3.1.1 Tin(II) precursors for the synthesis of tin chalcogenide

Divalent tin chalcogenolates (*e.g.*, $_\infty{}^1[Sn(EPh)_2]$ (E = S, Se, Te),[102] $[M(Sepy)_2]$,[97] $[Sn\{ESi(SiMe_3)_3\}_2]$ (E = S, Se, Te),[98] undergo a single step decomposition to yield ME with concomitant elimination of chalcogeno ethers. The complexes $_\infty{}^1[Sn(EPh)_2]$ start decomposing under a flow of helium gas at 265, 200 and 126 °C for E = S, Se, Te, respectively with the formation of phase pure SnE.[101] The complex $[Sn\{TeSi(SiMe_3)_3\}_2]$ either under flowing nitrogen at 250 °C or in refluxing toluene affords phase pure

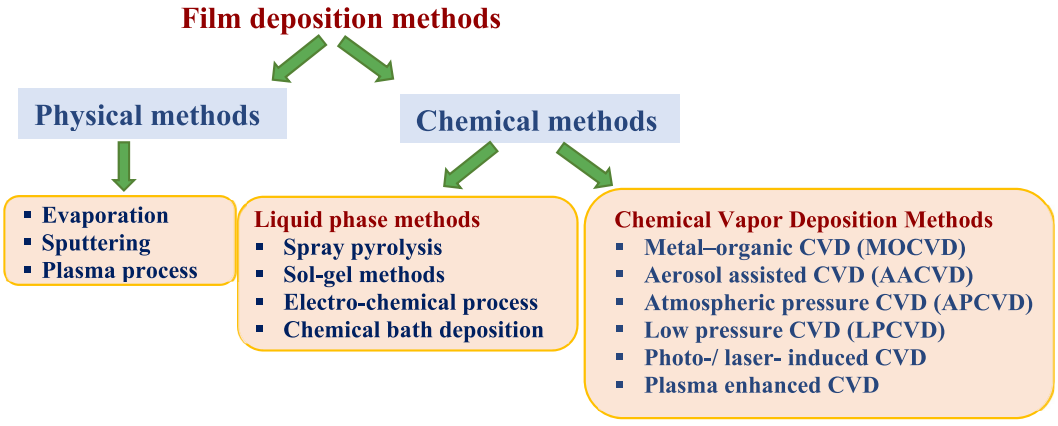

Scheme 3: Different deposition methods for metal chalcogenide thin films.

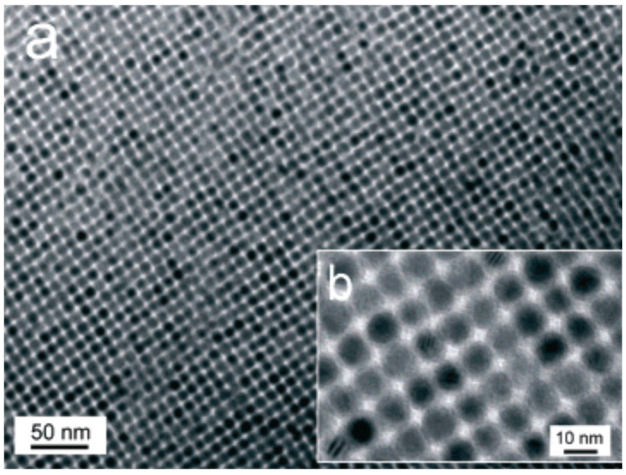

Figure 6: TEM images of as-synthesized SnTe NCs (10.2 nm) capped with oleic acid, (a) bar indicates 50 nm, (b) bar represents 10 nm. (Reproduced with permission from American Chemical Society[137]).

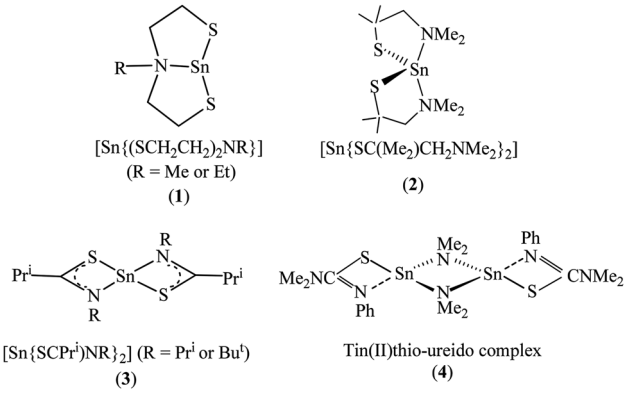

Scheme 4: Structures of tin(II)precursors used for the synthesis of tin chalcogenides.

SnTe, whereas other complexes, $[Sn\{ESi(SiMe_3)_3\}_2]$ (E = S or Se) under similar conditions yield SnE contaminated with metallic impurities.[98] Nanocrystals of cubic phase of SnTe have been isolated by rapidly injecting a mixture of $[Sn\{N\{SiMe_3\}_2\}_2]_2$ and trioctylphosphine telluride in ODE containing OLA at 150 °C.[102] These SnTe NCs in tetrachloroethylene when evaporated slowly under low pressure resulted in the formation of self-assembled superlattice (Figure 6). The size of NCs varied in the range 4.5–15 nm and can be managed by fine tuning the rate of injection, thermolysis temperature and concentration of OLA in the reaction. The optical band gap values for 7.2 and 14 nm NCs are 0.54 and 0.39 eV, respectively.[102]

Bis(3-mercapto-1-propanethiolato)tin(II), $[Sn(SCH_2CH_2CH_2SH)_2]$ has been employed to grow thin films of orthorhombic SnS in the temperature range 300–400 °C on glass substrates.[103] Films could be deposited in the absence of H_2S gas, unlike tin(IV) precursors, $Sn(SR)_4$ which required H_2S as an additional sulfur source (see later). The SnS films showed an optical band gap of ~1.31 eV. Tin(II) aminothiolate complexes, $[Sn\{(SCH_2CH_2)_2NR\}]$ (R = Me or Et) (**1**) (Scheme 4)[87] and $[Sn\{SC(Me_2)CH_2NMe_2\}_2]$ (**2**) (Scheme 4)[104] undergo a single step decomposition to give SnS. Microwave-assisted solvothermal decomposition of $[Sn\{(SCH_2CH_2)_2NMe\}]$ in N-methyl-2-pyrrolidone gave flake-like nanocrystals of SnS while the thermolysis of $[Sn\{SC(Me_2)CH_2NMe_2\}_2]$ in OLA at 270 °C afforded orthorhombic SnS nanocrystals. The complex $[Sn\{SC(Me_2)CH_2NMe_2\}_2]$ has also been used for growing thick and well-faceted orthorhombic SnS thin films on SiO_2 substrate at 300 °C.[104] Similarly, a toluene solution of tin(II) thioamidate, $[Sn\{SCPr^i)NR\}_2]$ (R = Pr^i or Bu^t) (**3**) (Scheme 4) has been used for growing SnS thin films on SiO_2-coated glass substrate in the temperature range 200–400 °C.[105] Another precursor, tin(II) thio-ureido (**4**) (Scheme 4) has been used for selective deposition of orthorhombic (α-SnS) and cubic zinc blende SnS (π-SnS) films of ~800 nm thickness on glass substrates by AACVD.[106] The TG analysis revealed a single step decomposition with an onset temperature of ~270 °C. The cubic phase SnS films were formed at 300 °C whereas orthorhombic SnS films were produced at higher temperatures (350–450 °C). These films showed optical band gaps of 1.78 and 1.34 $eV_{(direct)}$, respectively.[106] The photoelectrochemical analysis revealed that α-SnS films exhibited cathodic photocurrent (p-type behaviour) while π-SnS films showed both p- and n-type photocurrent behaviour. Mishra and coworkers synthesized a mononuclear tin(II) thiolate, $[Sn(SBu^t)(tfb\text{-}dmeda)]$ by the reaction of $[Sn(SBu^t)_2]$ with Htfb-dmeda which undergoes decomposition in a single step in the temperature range 250–275 °C.[107] Using this precursor, films of various thickness (80 nm – 2 μm) of orthorhombic SnS have been deposited on different supports, like FTO, Mo-coated soda lime glass, in the temperature range of 330–450 °C by CVD method.[107]

Tin(II) 1,1′-dithiolate/-diselenolate complexes have been used successfully as single source molecular precursors for the synthesis of tin chalcogenides.[108–111] The dithiocarbamate complexes, $[Sn(S_2CNRR')_2]$ (R/R' = Et/Et, Me/Bu^n, Et/Bu^n) undergo thermal decomposition in the temperature range 210–360 °C yielding SnS.[109,110] However, in coordinating solvents decomposition of $[Sn(S_2CNEt_2)_2]$ takes place at much lower temperatures. In hexadecyl amine or oleyl amine the complex decomposes at temperature as low as 85 °C yielding nanocrystals of orthorhombic SnS. The shape and size of NCs can be modified by the solvent, duration and temperature of thermolysis.[110] Interestingly, 1,10-phenanthroline adduct, $[Sn(S_2CNEt_2)_2(phen)]$, on the other hand can be employed for the preparation of two different tin sulfides, *viz.* SnS and SnS_2 by subtle variation in reaction parameters.[111] Thermolysis in a mixture of OLA and ODE (1:1 ratio) at 300 °C yields nanosheets (7 μm × 3 μm × 20 nm) of orthorhombic SnS which exhibits

electrochemical properties with capacity of 350 $mAhg^{-1}$ around 1.2 V. However, thermolysis at 280 °C in a mixture of OLA–OA-ODE (1:1:2 ratio) affords nanoplates (6 × 150 nm) of hexagonal SnS_2.[111] A 1,1′-diselenolato complex, $[Sn(Se_2PPh_2)_2]$ has been successfully employed for orthorhombic SnSe films deposition on borosilicate glass plates at 400 °C under a flowing argon atmosphere by AACVD method.[108]

3.1.2 Tin(IV) precursors for the synthesis of tin chalcogenides

Different classes of both classical and organotin(IV) chalcogenolates have been used for the synthesis of tin chalcogenides. Homoleptic tin chalcogenolates, *viz.*, $[Sn(SCH_2CF_3)_4]$,[112] $[Sn(SPh)_4]$,[113] $[Sn(SCH_2CH_2S)_2]$,[114] $[Sn(SePh)_4]$[115] and $[Sn(Sepy)_4]$,[97] on pyrolysis yield SnE or SnE_2 depending on the nature of the precursor. The thiolate complexes, $[Sn(SR)_4]$ (R = CH_2CF_3, Ph) and $[Sn(SCH_2CH_2S)_2]$ require H_2S as an additional source and yield different tin sulfides depending on the decomposition temperatures.[112–114] The complexes $[Sn(SR)_4]$ give SnS_2 at 300–450 °C and SnS at 500–600 °C[112,113] whereas $[Sn(SCH_2CH_2S)_2]$ at 350, 400 and 500 °C produces yellow SnS_2 (spherical particles of diameter 300 nm), brown Sn_2S_3 (needle like growth) and silver-grey SnS (overlapping plates of 2 × 2 µm), respectively thin films on glass substrates under AACVD conditions.[114] Penta- and hexa-coordinated tin(IV) selenolate complexes, $[SnCl_2\{(SeCH_2CH_2)_2NMe\}]$ and $[Sn\{(SeCH_2CH_2)_2NMe\}_2]$, respectively decompose in four steps to result in the formation of orthorhombic SnSe via $SnSe_2$ intermediate generated at lower temperatures. The bis complex either on thermolysis at 350 °C or on microwave-assisted thermolysis in N-methyl-2-pyrrolidone at 300 °C yields hexagonal plates of diameter ranging from 7.5 to 20 µm of $SnSe_2$.[116]

Pyrolysis of $[Sn(Sepy)_4]$ in a sealed tube at 300 °C gives $SnSe_2$ and py_2Se,[97] whereas $[Sn(SePh)_4]$ on thermolysis at 300 °C produced NCs of SnSe.[115] Similarly bis(chalcogenolates), $[Sn(EPh)_2\{N(SiMe_3)_2\}_2]$, obtained by oxidative addition of Ph_2E_2 on stannylene, $[Sn\{N(SiMe_3)_2\}_2]$, undergo single step decomposition (TGA) and on thermolysis in OLA at 210 °C yields nanocrystals of SnE (E = S, Se, Te). The size of NCs is influenced by duration of thermolysis.[117] For instance, the size of SnSe nanocrystals can vary from 60–90 nm, 0.5–1.0 µm and 250–500 nm, respectively for 20, 40 and 120 min. Reid and coworkers examined a series of butyltin chalcogenolates, $[Bu^n_3Sn(EBu^n)]$ (E = S, Se, Te) and $[Bu^n_2Sn(SBu^n)_2]$ as molecular precursors for growing thin films of SnE on silica plates by LPCVD techniques.[118,119] The complexes, $[Bu^n_3Sn(EBu^n)]$ (E = Se, Te) and $[Bu^n_2Sn(SBu^n)_2]$ produced orthorhombic SnE (E = S or Se) and cubic SnTe films, but $[Bu^n_3Sn(SBu^n)]$ gave sulfur deficient SnS films. Cubic SnTe films were found to be p-type semiconductor. Their temperature dependent thermoelectric performance revealed peak Seebeck coefficient of 78 μVK^{-1} and power factor of 8.3 $\mu WK^{-2}\,cm^{-1}$ at 342 °C.[119]

Authors' group[120–129] has developed diorganotin(IV) complexes derived from N-heterocyclic chalcogen ligands (Scheme 5) as molecular precursors. The complexes have been examined by NMR spectroscopy and single crystal X-ray diffraction analyses. These complexes have been successfully used for the synthesis of phase pure tin chalcogenides (SnE and SnE_2) either in NC form or for growing thin films without any requirement of additional chalcogen source.

A number of diorganotin 2-pyridyl/2-pyrimidylthiolates, $[R_2Sn(Spy)_2]$ (R = Me, Et, Bu^t), $[R_2Sn(Cl)(Spy)]$ (R = Et, Bu^t) and $[R_2Sn(Cl)(SpymMe_2)]$ (R = Me, Et, Bu^t) on thermolysis through heat-up approach in OLA at 240 °C yields hexagonal nanosheets (thickness of 30–80 nm) (*e.g.* from $Et_2Sn(Spy)_2$]) and rectangular sheets (301 × 390 × 58 nm) (*e.g.* from $[Et_2Sn(Cl)(SpymMe_2)]$) of orthorhombic SnS with direct band gap of 1.61–1.90 eV.[124,129] Morphology and crystallite size of nanosheets of SnS produced from $[Bu^t_2Sn(SpymMe_2)_2]$ in high boiling coordinating solvents (oleyl amine, octadecene, dodecane thiol), can be controlled by the reaction solvent.[122] For instance, SEM and TEM images of SnS prepared in OAm (Figure 7a and b) depicts rectangular nanosheets while those produced in DDT reveal a mixture of rectangular and hexagonal sheets (Figure 7d and e). On contrary, SnS obtained in ODE exhibit irregular nanosheets (Figure 7g and h). The interplanar spacing depicted in the respective HRTEM images point to orthorhombic SnS (Figure 7c, f and i). The thickness of these SnS nanosheets vary depending on the precursor employed in the thermolysis. For instance, the thickness of SnS nanosheets was around 50 nm in the case of $[^tBu_2Sn(Spy)_2]$ while dimensions of nanoplatelets obtained by thermolysis of $[^tBu_2SnCl(Spy)]$ is larger due to relatively faster growth kinetics of nanoplatelet formation.[129] These precursors have also been utilized for the deposition of orthorhombic SnS thin films on glass and silicon substrates at 400 °C through AACVD. Microscopic images unveiled randomly oriented rectangular blocks and hierarchical flowers on the glass and silicon substrates. The

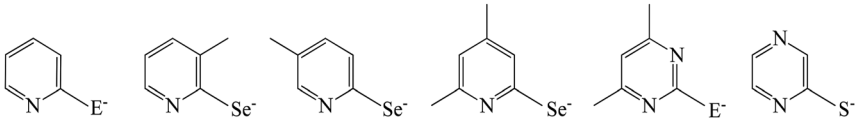

Scheme 5: N-Heterocyclic chalcogenolate ligands (E = S or Se).

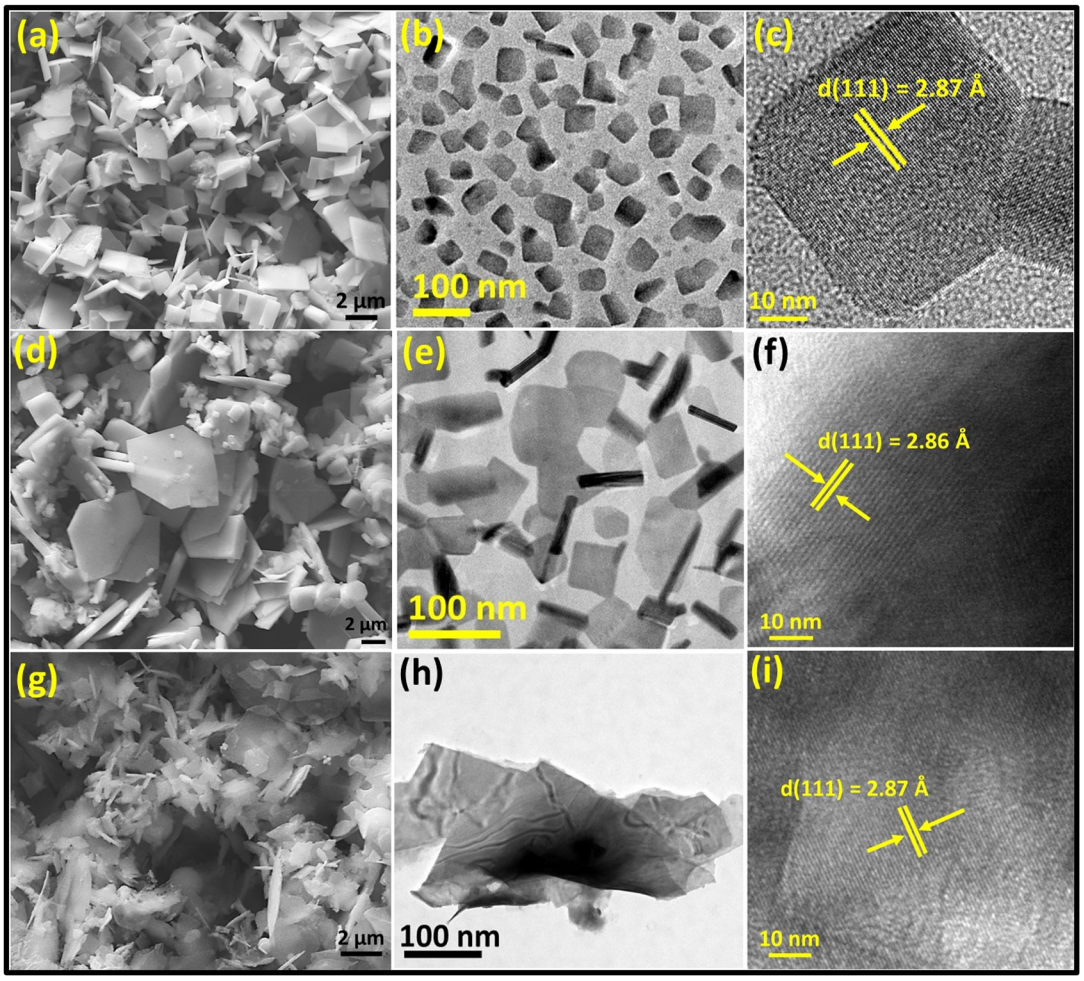

Figure 7: SEM, TEM and HRTEM images of orthorhombic SnS nanostructures synthesized by the thermolysis of [^{t}Bu$_2$Sn(SpymMe$_2$)$_2$] at 250 °C for 10 min in (a–c) OAm, (d–f) DDT and (g–i) ODE, respectively (Reproduced with permission from Elsevier[122]).

morphological difference of SnS with respect to nature of the substrate has been ascribed to the orientation and interaction of the substrate atoms with the droplets of the precursor approaching the substrate surface.[124] Similarly, thermolysis of [^{t}Bu$_2$Sn(Spyz)$_2$] (HSpyz = 2-pyrazinyl thiol) in OLA at 300 °C gave rectangular sheets (size ~30 nm) of orthorhombic SnS.[128]

Diorganotin 2-pyridyl, 3-methyl-2-pyridyl and 5-methyl-2-pyridyl, 4,6-dimethyl-2-pyridyl and 4,6-dimethyl-2-pyrimidyl selenolates undergo clean thermolysis in OLA to give different morphologies of orthorhombic SnSe (*e.g.* from [Me$_2$Sn(Sepy)$_2$], [Me$_2$Sn(SepyMe$_2$)$_2$]) or hexagonal SnSe$_2$ (*e.g.* from [R$_2$Sn(SepymMe$_2$)$_2$]) nanoparticles depending on the nature of precursor.[121,123,125,126] For example, different nanostructures of tin selenide can be prepared by [^{t}Bu$_2$Sn{SeC$_5$H$_3$(Me-5)N}$_2$] on injecting in different solvent systems (ODE, OLA, OA or in 1:1 (v/v) ODE:OLA and OA:OLA).[126] Thermolysis of [^{t}Bu$_2$Sn{SeC$_5$H$_3$(Me-5)N}$_2$] in ODE and OLA yield hexagonal sheets of hexagonal phase SnSe$_2$ and irregular sheets of orthorhombic SnSe (average thickness 18 and 12 nm), respectively. While in OA and in solvent mixtures (ODE:OLA and OA:OLA), a mixture of sheets of different shapes could be obtained. The nanoflakes of thickness as tiny as 10 nm are formed in OA:OLA mixture which has been attributed due to stronger binding of the oleate group. The complex, [Bu$_2^t$Sn(Sepy)$_2$] has been employed to deposit films of orthorhombic SnSe on glass and p-type silicon(100) substrates at substrate temperature 490 °C. Similarly photo-responsive nanosheets of SnSe$_2$ can be deposited from [Bu$_2^t$Sn(SepyMe-5)$_2$].[126] The complex [Bu$_2^t$Sn(SepymMe$_2$)$_2$] has been engaged to coat SnSe$_2$ thin films on silicon wafers at 375 °C by AACVD. The direct band gaps of as deposited and annealed thin films are 2.12 and 2.06 eV, respectively.[125] The optical band gaps (direct band gaps for SnSe 1.68–1.78 eV[121] and for SnSe$_2$ 1.76–2.30 eV[125]) of these nanostructures are blue shifted with reference to bulk material indicative of quantum confinement.

1,1′-Dithiolate complexes of tin(IV) are yet another family of precursors employed for the synthesis of tin sulfide NCs and for thin films deposition.[130–134] Heteroleptic dithiocarbamates, $[Sn(SR)_2(S_2CNEt_2)_2]$ (R = CH_2CF_3, c-Hex) on heating undergo reductive elimination of disulfide (R_2S_2) with concomitant formation of tin(II) complex, $[Sn(S_2CNEt_2)_2]$ which after subsequent loss of $(Et_2NCS)_2S$ yields SnS.[131] In contrast, tetrakis derivative, $[Sn(S_2CNEt_2)_4]$ takes a different decomposition path.[131] The complex starts decomposing either on leaving in $CHCl_3/CH_2Cl_2$ at RT or on heating at 200 °C to a dimeric sulfido-bridged complex, $[Sn(\mu\text{-}S)(S_2CNEt_2)_2]_2$, which on further heating to 375 °C leads to the formation of hexagonal SnS_2.[131] Organotin dithiocarbamates, $[Me_3Sn(S_2CNMeBu^n)]$ and $[Bu^nSn(S_2CNMeBu^n)_3]$, on the other hand, requires H_2S as additional sulfur source when used for growing thin films of SnS.[132] In the absence of H_2S gas no films could be grown.[132] In contrast, dibutyltin dithiocarbamates, $[Bu_2Sn(S_2CNRR')_2]$ (R/R' = Et/Et; Me/Bu^n; Bu^n/Bu^n; Me/*n*-Hex), in the absence of H_2S gas, could produce orthorhombic SnS films on glass substrate in the temperature range 400–530 °C by AACVD method.[134] The films consisted of sheet-like crystallites and the presence of a small amount of SnO_2. The nature of precursor and deposition temperature greatly influenced the band gap of the films which varied in the range 1.21–1.71 eV and the photo-sensitivity varied from 0.4 to 2.1 % for films deposited at 500 °C.[134] Thermolysis of dibutyltin bis(piperidine dithiocarbamate), $[Bu_2Sn\{S_2CN(CH_2)_5\}_2]$ in OLA at 230 °C yields nanosheets (998 × 465 nm) of phase pure orthorhombic SnS.[133] Like dibutyltin dithiocabamates, diphenyltin xanthates, $[Ph_2Sn(S_2COR)_2]$ (R = CH_2CH_2OMe, Bu^i) behave similarly.[130] SnS films deposited using these precursors on glass substrates in 400–575 °C range by AACVD were contaminated with some SnO_2.[130] Thio-/seleno-benzoate complexes, $[Bu_2Sn(ECOPh)_2]$ (E = S or Se) have been used for the preparation of orthorhombic SnE.[135,136] OLA capped nanosheets of SnSe have been prepared by hot injection method by injecting TOP dispersion of selenobenzoate complex to preheated OLA at 200 °C. Thin films of SnSe could also be grown on a glass substrate using a THF solution of the complex by AACVD. Uniform deposition of crystalline films takes place in the temperature range 375–475 °C.[135]

Organotin chalcogenides have also been investigated as SSMPs for tin chalcogenides. Boudjouk and coworkers employed diorganotin chalcogenides, $[(R_2SnE)_3]$ (R = Ph or Bz; E = S or Se)[94,137] and bis(triorganotin) chalcogenides, $(R_3Sn)_2E$ (R = Ph or Bz; E = S, Se, Te)[94,138] as molecular precursors for the synthesis of SnE. Pyrolysis of $[(R_2SnE)_3]$ under an inert atmosphere yields NCs of phase pure orthorhombic SnE (E = S or Se).[94,137] Pyrolysis of $(Ph_3Sn)_2E$ under flowing nitrogen in a tube furnace at above 330 °C yields a dark grey powder of micro-crystalline orthorhombic phase of SnE (E = S or Se) and cubic SnTe.[138] In contrast, the corresponding benzyltin derivatives, $(Bz_3Sn)_2E$ (E = S or Se) yield SnE contaminated with some elemental tin.[94] Flow pyrolysis of structurally characterized dibenzyltin telluride, $[(Bz_2SnTe)_3]$ at 200–275 °C affords phase pure cubic SnTe nanocrystals of size ~1 μm.[139] Chalcogenido-bridged diorganotin complexes, $[Sn(\mu\text{-}E)\{CH(SiMe_3)_2\}_2]_2$ (E = S, Se, Te) (**5**) (Scheme 6), obtained by oxidative addition of chalcogen on tin(II) compound $[Sn\{CH(SiMe_3)_2\}_2]$, are thermally quite stable.[140,141] Only tellurido-bridged complexes undergo decomposition and could be used for growing SnTe films on gold seeding layers

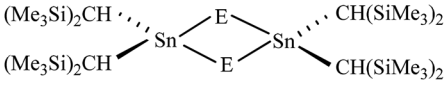

$[Sn(\mu\text{-}E)\{CH(SiMe_3)_2\}_2]_2$ (E = S, Se, Te)

(**5**)

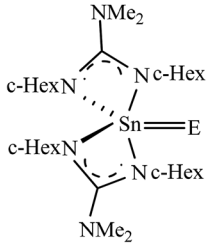

$[E{=}Sn\{(N\text{-}c\text{-}Hex)_2CNMe_2\}_2]$
(E = S, Se, Te)

(**6**)

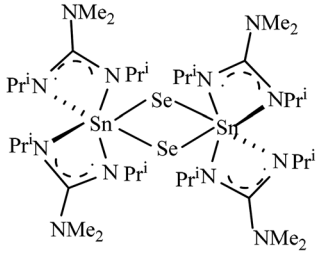

$[Sn(\mu\text{-}Se)\{Me_2NC(NPr^i_2)_2\}_2]_2$

(**7**)

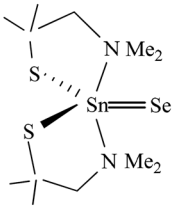

$[Sn^{IV}(dmampS)_2Se]$
(dmampS =1-(dimethylamino)-2-methylpropane-2-thiolate

(**8**)

Scheme 6: Some representative tin(IV) precursors used for the synthesis of tin chalcogenides.

at 400 °C.[140] Similarly other tin(IV) chalcogenide complexes (**6–8**) (Scheme 6) were obtained by oxidative addition of chalcogen on tin(II) complexes.[86,104,142] The complexes **6** can also be prepared by salt metathesis reaction between [Sn{(N-c-Hex)$_2$CNMe$_2$}$_2$Br$_2$] and Li$_2$E[86] which on thermolysis in OLA at 210 °C yields nanocrystals of SnE.[86]

Reid and coworkers employed Lewis acid-base adducts of the type *trans*-[SnCl$_4$(ER$_2$)$_2$] (E = S or Se; R = Et or Bu^n) and *cis*-[SnCl$_4$(RE$^\frown$ER)] (E = S or Se; RE$^\frown$ER = Bu^{n}E(CH$_2$)$_n$EBu^n (*n* = 2 or 3); *o*-(MeECH$_2$)$_2$C$_6$H$_4$) for deposition of tin chalcogenide thin films of various thickness on different substrates (Si; SiO$_2$; TiN) using LPCVD methods.[143–145] Depending on precursor and decomposition temperatures, films of different tin chalcogenides could be grown. Complexes with chelating ligands decompose at higher temperatures with respect to those containing monodentate ligands.[144,145] In general, at lower deposition temperatures SnE$_2$ is preferentially formed whereas at higher temperatures films of SnE are formed. For instance, *cis*-[SnCl$_4$(Bu^{n}E(CH$_2$)$_3$EBu^n)] at 286 and 480–500 °C gave SnS$_2$ and SnSe$_2$, respectively, but at 558 and 588 °C produced SnS and SnSe.[144] Boscher et al. instead of Lewis acid-base adducts, employed dual source – SnCl$_4$ and Et$_2$Se for growing thin films of SnSe and SnSe$_2$ on glass substrate under LPCVD conditions.[146] SnSe films (100 nm thick) could be deposited at 650 °C whereas SnSe$_2$ films of 10–80 μm size adherent crystals were formed at 600-650 °C.[146] Similarly, the dual source approach using SnCl$_4$ and H$_2$S, has been used to deposit different tin sulfides depending on the deposition temperatures. Thus, films of hexagonal SnS$_2$, orthorhombic Sn$_2$S$_3$ mixed with some SnS$_2$ and orthorhombic SnS could be deposited on glass substrate by APCVD method at 500, 525 and 545 °C, respectively.[147] The use of dual source precursors for growing thin films can be traced back to 1970s when Manasevit and Simpson deposited SnE (E = S, Se, Te) films on various substrates using tetramethyl tin and H$_2$S/H$_2$Se/Me$_2$Te under a flow of hydrogen at 550, 500 and 650 °C, respectively.[148] Besides chalcogeno ether adducts, adducts of other chalcogen ligands, like thiosemicarbazone (*e.g.*, [Bz$_3$Sn(Cl){S=C(NH$_2$)NH–N(=CHAr)}], where Ar = 2-HOC$_6$H$_4$; 4-ClC$_6$H$_4$),[149] N,N-dimethyl selenourea (*e.g.*, [SnCl$_4${Se=C(NMe$_2$)NH$_2$}$_2$]),[87] have also been explored as templates for tin chalcogenides. The selenourea complex, [SnCl$_4${Se=C(NMe$_2$)NH$_2$}$_2$] undergoes a two-step decomposition. It yields SnSe$_2$ at 400 °C (from TGA), but thermolysis either in OA or in an OA-OLA mixture at 350 °C produces nano-flakes of a mixture of SnSe and SnSe$_2$.[87]

3.2 Synthesis of ternary tin chalcogenides

Three different families of ternary tin chalcogenide materials, *viz.* anion- and cation-alloyed IV-VI materials (SnE$_x$E'$_y$ and Sn$_{1-x}$-IV$_x$-E) and M$_x$Sn$_y$E$_z$, can readily be identified, the latter being the most extensively studied semiconductors.

3.2.1 SnE$_x$E'$_y$ materials

The optical band gap and thermal conductivity of binary tin chalcogenides can be further fine-tuned in anion-alloyed ternary systems for their thin-film based solar-cell and thermoelectric applications. These materials can be generated by direct heating of stoichiometric quantities of constituent elements,[150] by heat-up method[151] or by molecular precursor route.[94,152,153]

Organotin chalcogen compounds have been effectively probed as precursors for the synthesis of anion-alloyed materials. Pyrolysis of a mixture of [Bz$_2$SnS]$_3$ and [Bz$_2$SnSe]$_3$ in different molar ratios at 450 °C afforded ternary tin chalcogenides, SnS$_{0.75}$Se$_{0.25}$, SnS$_{0.5}$Se$_{0.5}$ and SnS$_{0.25}$Se$_{0.75}$, respectively as plate-shaped (~4 μm) NCs.[94] The entire range of SnS$_{1-x}$Se$_x$ has been prepared by thermolysis of bis(thiobenzoato)dibutyltin(IV) and bis(selenobenzoato)dibutyltin(IV) in an appropriate molar ratios in OLA at 230 °C. A steady variation in the band gap on going from SnS (1.48 eV) to SnSe (1.1 eV) has been observed as revealed by UV-Vis-NIR analysis.[136]

Oxidative addition of chalcogen on organotin(II) chalcogenides, (RSn)$_2$X yields (RSnE)$_2$X (R = 2,6-(Me$_2$NCH$_2$)$_2$C$_6$H$_3^-$; X = S, Se and E = S, Se, Te) (Scheme 7)[152,153] which serve as a single source precursors for ternary tin selenides. These compounds contain two terminal Sn = E bonds[153] and decompose in multiple steps to give tin chalcogenides. Thermolysis of (RSnSe)$_2$S yields SnS$_{0.5}$Se$_{0.5}$ whereas (RSnTe)$_2$X (X = S or Se) gives only SnTe as the main product. However, SnSe$_x$Te$_{1-x}$ (x = 0–0.15) has been prepared by

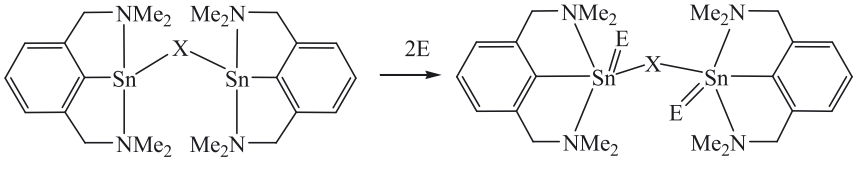

X	E
S	Se
S	Te
Se	Te

Scheme 7: Oxidative addition of chalcogen on organotin(II) complexes.

heating pure elemental Sn, Se and Te in stoichiometric amounts in a sealed quartz tube at 900 °C.[150]

The band gap of SnS_xSe_{1-x} nanocrystals (7–15 nm), obtained by hot injection method employing an ODE–OA solution of SnO treated with the solutions of TOP/Se and OLA/S at 270 °C, can be tuned from 0.92 to 1.24 eV with a linear change of S/(S + Se) and fall within the range of band gaps of SnS (1.6 eV) and SnSe (1.1 eV).[154] The band gap energy can effectively be modulated in a wide range of 0.96–2.26 eV in SnS_xSe_{1-x}, $Sn(S_xSe_{1-x})_2$, and Sn_2S_3 NCs (Figure 8).[155] Thin films of semiconducting SnSSe material have been deposited by spin-coating methods at varying spinning speeds. For instance, amorphous films of $Sn_{42}S_{41}Se_{17}$ with an optical band gap of 1.79 eV are deposited at 1,500 rpm.[153] Thin films deposited using a hydrazine solution of SnS_2, $SnSe_2$ and sulfur followed by annealing at 270 °C had the composition $SnS_{2-x}Se_x$.[151] These films exhibited n-type transport properties with large current densities greater than 10^5 A cm^{-2} and mobilities higher than 10 cm^2 V^{-1} s^{-1}.

3.2.2 Sn_{1-x}-IV_x-E materials

A number of cation-alloyed ternary IV–VI group semiconductors have been synthesized by several methods. Earlier methods relied on direct heating of stoichiometric quantities of constituent elements in sealed ampules (such as $Sn_xGe_{1-x}Se$ ($0 \le x \le 1$)) at high temperatures,[156] but the current methods employ solution techniques. Nanocrystals of $Sn_xGe_{1-x}Se$ ($0 \le x \le 1$) have been prepared by injecting a hexamethyldisilazane solution of $Bu^t{}_2Se_2$ into hot (95 °C) dodecyl amine solution of GeI_4 and SnI_4 mixture in a desired ratio and heating further at 225 °C.[157] Powder X-ray diffraction patterns of $Sn_xGe_{1-x}Se$ ($0 \le x \le 1$) point out orthorhombic *Pmna* crystal structure for these nanocrystals (Figure 9). The indirect band gap energy of these NCs varied in the range 0.87–1.13 eV as a function of x = 1.0–0.2. Nanosheets of $SnGeS_3$ have been isolated by thermolysis of xanthate complexes,

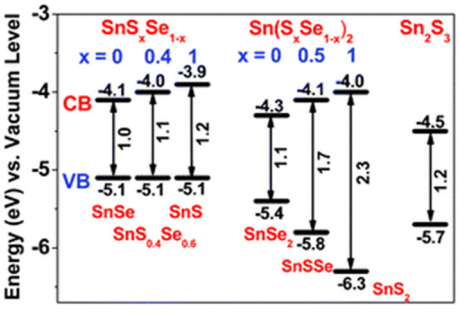

Figure 8: Schematic representation of band gap energy of SnS_xSe_{1-x}, $Sn(S_xSe_{1-x})_2$, and Sn_2S_3 NCs (reproduced with permission from Royal Society of Chemistry[155]).

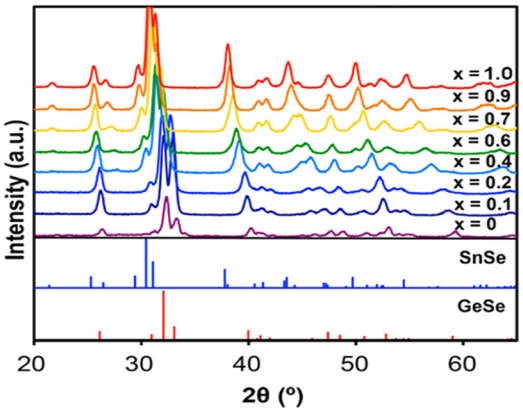

Figure 9: XRD patterns of $Sn_xGe_{1-x}Se$ nanocrystals with different compositions. (Reproduced with permission from American Chemical Society[157]).

$[M(S_2COPr^i)_4]$ (M = Ge and Sn). These photo-responsive nanosheets exhibit a band gap of 1.59 eV as measured from diffuse reflectance spectroscopy (DRS).[158]

Ternary $Pb_{1-x}Sn_xE$ compounds are narrow band gap semiconductor materials. They exist in a cubic rock salt crystal structure. Nanocrystals of $Pb_{1-x}Sn_xS$ (av. size 8 nm) have been isolated by solvothermal route. In this method an OLA solution of sulfur is swiftly added to a hot solution of a mixture of stannous oxide and lead oxide in ODE and OA and heated further at 270 °C. The band gap (1.57 (when x = 0.54) to 1.96 eV (when x = 0.85)) varied nearly linearly with the gradual rise of Pb/(Pb + Sn) ratio.[159] A series of $Pb_{1-x}Sn_xTe$ nanocrystals (~7.5 nm in size) have been synthesized by the reaction of lead oleate and $[(Me_3Si)_2N]_2Sn$ mixture with a TOP solution of tellurium at 150 °C. These NCs unveil band gaps in the mid-IR region. TEM images of the pristine $Pb_{1-x}Sn_xTe$ NCs are nearly spherical with the average particle size varying between 6.0 and 8.7 nm irrespective of all compositions (Figure 10). Here, $Pb_{0.86}Sn_{0.14}Te$ and $Pb_{0.14}Sn_{0.86}Te$ NCs are monodispersed and spherical in shape while the morphology of $Pb_{0.5}Sn_{0.5}Te$ NCs varies from spherical to oval and are polydispersed in nature. The change in morphology of NCs has been attributed due to the different binding affinity of Pb and Sn precursors with oleic acid and amine moieties.[160]

3.2.3 $M_xSn_yE_z$ materials

Various synthetic methods for the NCs of Cu_2SnE_3 (E = S,[56,161–163] Se[67,164–170]) have been reported and include heat-up, hot-injection, solvothermal/hydrothermal routes. Reactions in these synthetic routes are carried out in different solvents, like OLA, ODE, OA, HDA, TOPO, using a range of copper (CuCl, CuI, $CuCl_2$, $Cu(acac)_2$) and tin ($SnCl_2$, $SnBr_2$, $SnCl_4$, $Sn(acac)_2$,

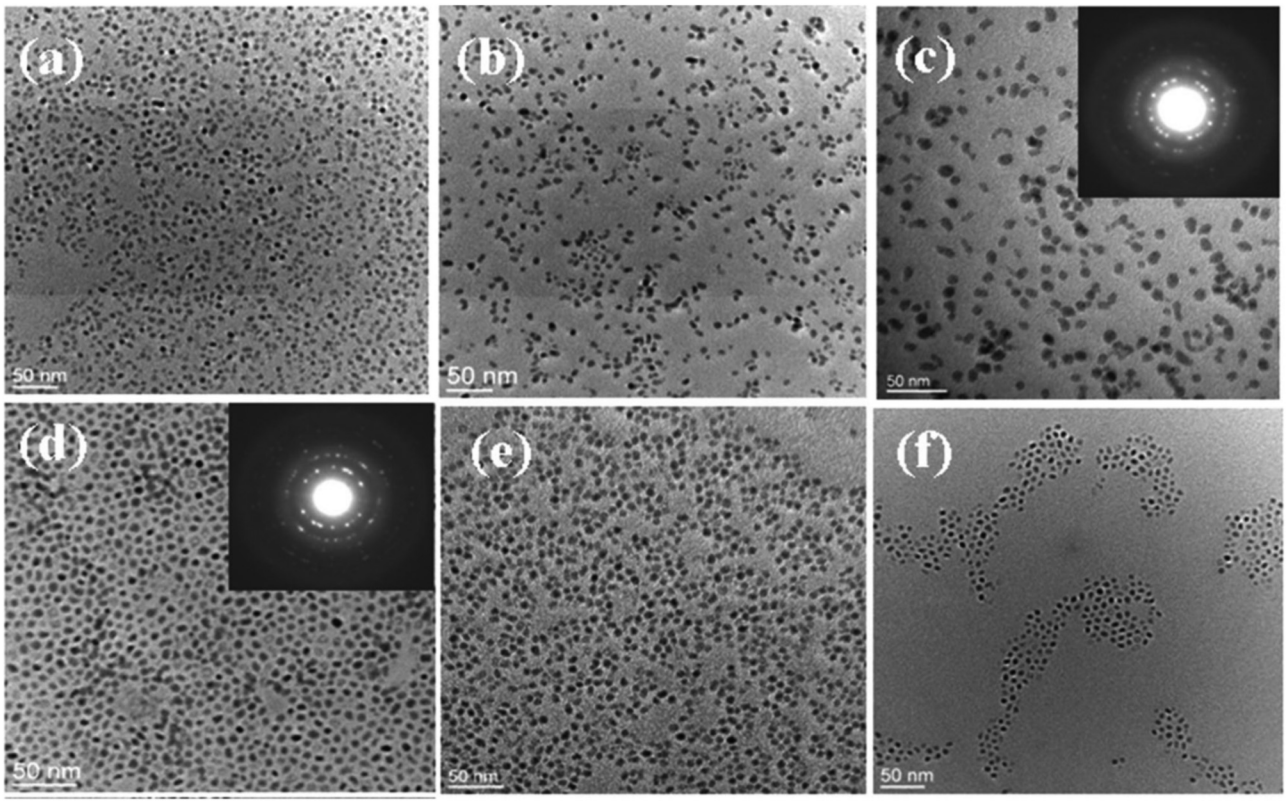

Figure 10: TEM images of the (a) $Pb_{0·86}Sn_{0·14}Te$, (b) $Pb_{0·8}Sn_{0·2}Te$, (c) $Pb_{0·5}Sn_{0·5}Te$, (d) $Pb_{0·33}Sn_{0·67}Te$, (e) $Pb_{0·2}Sn_{0·8}Te$ and (f) $Pb_{0·14}Sn_{0·86}Te$ NCs. (Reproduced with permission from American Chemical Society[160]).

$Sn(OAc)_2$) precursors and a chalcogen source (S, Se, SeO_2, DDT, thio-/seleno-urea, $Bu^t_2Se_2$, Ph_2Se_2).[171] Several factors like metal precursor reactivity, nature of chalcogen source, reaction medium, and the reaction temperature, have a strong impact on the phase of the NCs. The use of different sulfur sources can give different phases. NCs of Cu_2SnS_3 synthesized by hot-injection route using an ODE solution of CuCl and $SnCl_2$ on treatment with OLA solution of sulfur at 240 °C affords the zinc blende phase, whereas treatment with dibutyldithiocarbamic acid (DBDCA) in ODE with a suitable capping agent (DDT, TOPO, OA) results in the formation of wurtzite phase.[172] Formation of different phases of Cu_2SnS_3 NCs in the reaction of CuI, $Sn(OAc)_2$ with DDT could be managed by proper selection of solvent. The use of ODE at 220 °C results in the formation of zinc blende phase whereas in OLA at 190 °C wurtzite phase of NCs is formed.[173]

Hot injection method has been frequently used for the preparation of Cu_2SnSe_3 NCs. Wang et al. from the reaction of CuCl, $SnCl_2$ in oleyl amine with Ph_2Se_2 at 310 °C isolated NCs of Cu_2SnSe_3 as tetrapods consisting of cubic core with four wurtzite arms.[67,170] Brutchey and co-workers[169] synthesized NCs (15.1 ± 2.9 nm) of wurtzite phase by treatment of a dodecyl amine-DDT solution of CuCl and SnI_4 with di-*tert*-butyl-diselenide ($Bu^t_2Se_2$). In these reactions, different phases could be conveniently controlled by suitable choice of capping agent and reaction temperatures.[169,170] Different crystal phases, cubic, zinc blende, hexagonal, wurtzite and monoclinic with varied morphologies of CTSe could be isolated by slight variation in the reaction parameters.[174] The wurtzite/monoclinic phase is typically formed at lower temperatures but on increasing the temperature the cubic phase is obtained.[174,175]

Authors' group employed organotin precursors for the synthesis of Cu_2SnE_3 (E = S or Se) (Figure 11).[127,128] Thermolysis of $[Bu^t_2Sn(Spyz)_2]$ and $[Cu(Spyz)(PPh_3)_2]$ (HSpyz = 2-mercapto pyrazine) in 1:2 ratio in OLA at 300 °C yields nanocrystals (~22 nm) of phase pure monoclinic Cu_2SnS_3. However, thermolysis either at lower temperatures or in a mixture of OLA-OA gave monoclinic CTS slightly contaminated with binary sulfides.[128] The band gaps of Cu_2SnS_3 nanostructures (1.4 eV) are blue shifted relative to bulk counterparts. Similarly, co-thermolysis of $[Cu(SepyMe\text{-}3)]_4$ and $[Me_2Sn(SepyMe\text{-}3)_2]$ in 1:2 M ratio in OLA or TOPO at 300 °C produced cubic Cu_2SnSe_3 nano-crystals (11 ± 1 nm). These NCs could be isolated in flower-shaped, dish-like, nano-sheets, polyhedra morphologies by subtle variation in

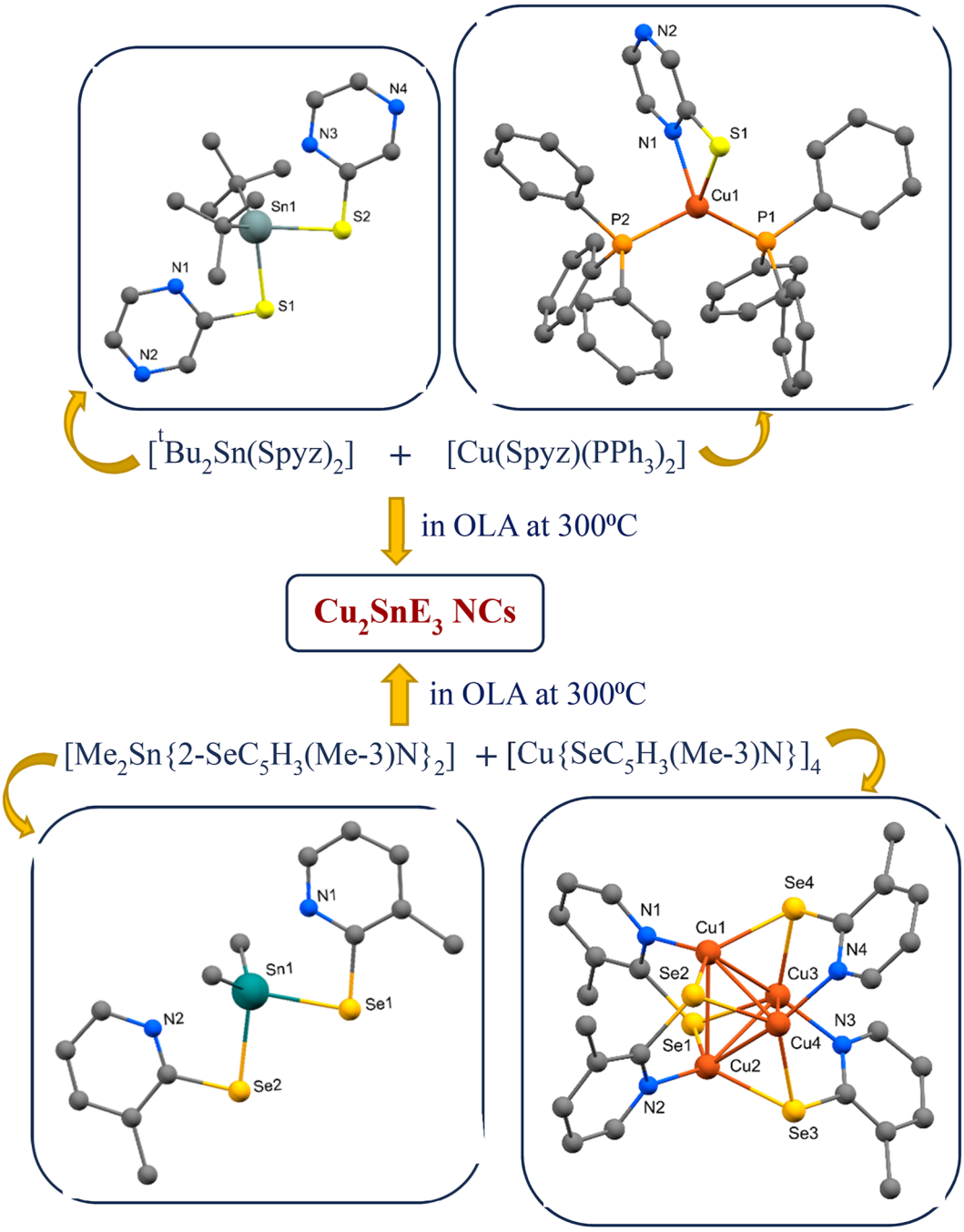

Figure 11: Synthesis of Cu_2SnE_3 (E = S or Se) NCs via organometallic precursor route (structures are drawn using Mercury Program (Mercury: Visualization and analysis of crystal structures).[127,128,176]

the reaction conditions. For instance, SEM of Cu_2SnSe_3 isolated by hot injection of $[Me_2Sn(SepyMe\text{-}3)_2]$ and $[Cu(SepyMe\text{-}3)]_4$ in OLA at 300 °C revealed polyhedra shape of NCs (Figure 12).[127]

O'Brien and coworkers deposited thin films of cubic Cu_2SnSe_3 using a THF solution of $Cu(acac)_2$ and $[Sn(Se_2PPh_2)_2]$ in 2:1 stoichiometric ratio by AACVD at 400 and 450 °C. Films grown at 400 °C consisted of nanocrystalline flakes of CTSe while those deposited at 450 °C consisted of semi-spherical crystallites.[108]

Nanocrystals of Cu_3SnS_4 have been isolated by hot injection and solvothermal methods. Orthorhombic Cu_3SnS_4 NCs (31.8 ± 4.9 nm) and nanosheets (15 nm thick with a lateral dimension of 209 ± 33 nm) have been prepared by

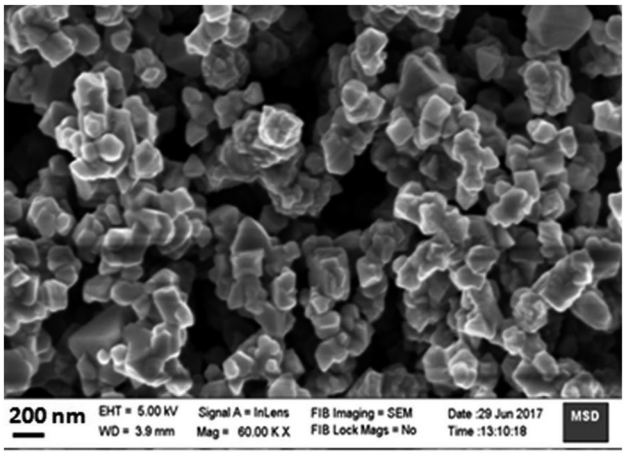

Figure 12: SEM image of Cu_2SnSe_3 polyhedra obtained by hot injection of $[Me_2Sn(SepyMe\text{-}3)_2]$ and $[Cu(SepyMe\text{-}3)]_4$ in OLA at 300 °C. (Reproduced with permission from Springer Nature Publishers[127]).

hot-injection route employing $Cu(acac)_2$, $SnCl_4$, followed by either seeding with monoclinic $Cu_{31}S_{16}$ NCs or by adding DDT.[177]

$ZnSnS_3$ is another interesting material. It exists in three closely related phases, *viz.* non-polar monoclinic and ilmenite and a polar lithium niobate (LN) form. The latter with a band gap of 1.28 eV exhibits ferroelectric behaviour.[178] Being a material with a narrow band gap, it is highly effective in countering the major limitation of traditional ferroelectric PV devices which employ oxide materials that have large band gaps (>3 eV). The films of LN-$ZnSnS_3$ and LN-$ZnSnS_3$@rGO have been prepared by hydrothermal method using $ZnSn(OH)_6$ and thiourea.[179,180]

The compound In_4SnSe_4 (band gap = 1.6 eV) is another narrow band gap ternary system. Nanowires (length 5–20 µm and width 100–400 nm) of In_4SnSe_4 have been prepared by heat-up method using $SnCl_2$, $InCl_3$, and Ph_2Se_2 in a mixture of ODE and OLA containing excess hexamethyldisilazane at 300 °C.[181]

3.3 Synthesis of quaternary tin chalcogenides

The interest in quaternary materials, I_2-II-IV-VI_4 (I = Cu, Ag; II = Zn, Cd, Hg; IV = Si, Ge, Sn; and VI = S, Se, Te) gained momentum around 2007 due to their numerous technological applications.[171,182] These quaternary materials are derived from substitution of cations in binary II-VI materials which adopt two crystallographic structures, *viz.* zinc blende (ZB) and Wurtzite (WZ). The most widely investigated quaternary systems are Cu_2ZnSnS_4 (CZTS) and $Cu_2ZnSnSe_4$ (CZTSe), although various other materials like $Cu_2ZnSnTe_4$, Cu_2CdSnS_4, $Cu_2CdSnSe_4$, Cu_2MSnS_4 (M = Mn, Fe, Co, Ni) have also been studied. As the number of constituent elements increases, synthesis of compositionally pure and single phasic quaternary systems becomes as elusive as complex. In such cases selection of precursors, ligands, solvents and reaction parameters are of paramount importance in order to avoid the formation of binary/ternary phases.

3.3.1 Synthesis of Cu_2ZnSnE_4 (E = S or Se)

Although there are several synthetic approaches to prepare Cu_2ZnSnS_4 (CZTS), to isolate high-quality stoichiometric materials over a large area remains a challenging task. Synthetic strategies employed for the preparation of CZTS include hydrothermal/solvothermal,[183,184] hot-injection method,[60,66,185,186] heating-up method, ultrasound-assisted microwave,[187] etc., hot-injection method being the most common technique. In these synthetic methods stoichiometric quantities of metal salts of copper ($CuCl_2{\cdot}2H_2O$, $Cu(OAc)_2.H_2O$, $Cu(acac)_2$), zinc ($ZnCl_2$, $Zn(OAc)_2.2H_2O$, $Zn(acac)_2$) and tin ($SnCl_2{\cdot}2H_2O$, $SnCl_4{\cdot}5H_2O$, $Sn(OAC)_4$) are dissolved in a suitable solvent (ethylene glycol, OLA, ODE, TOPO, monoethanolamine, etc.) and then treated with a sulfur source like elemental sulfur in OLA, thiourea, or thiols (DDT, *tert*-dodecane thiol). Alternatively, metal and the sulfur source can be substituted by metal complexes derived from sulfur ligands like diethyldithiocarbamate[1,188–191] and xanthates.[192] Diethyldithiocarbamate complexes, $[Cu(S_2CNEt_2)_2]$, $[Zn(S_2CNEt_2)_2]$ and $[Sn(S_2CNEt_2)_4]$ on thermolysis in oleyl amine/trioctyl amine have been successfully used to prepare NCs of CZTS.[1,190,191] Capping agents like OA,[1,193] hexadecane thiol,[190] are quite often employed to stabilize the NCs. For instance, Lu et al. generated wurtzite CZTS nano-prisms of size of 20 × 28 nm and nanoplates of thickness 14 nm in DDT/OLA and DDT/OA, respectively (Figure 13). Nanostructured thin films of CZTS have been grown by air spraying a THF solution of $Cu(S_2CNEt_2)_2$, $[Zn(S_2CNEt_2)_2]$ and $[Sn(^tBu)_2(S_2CNEt_2)_2]$ in 2: 1: 1 M ratio on a heated (450 °C) glass substrate under an argon atmosphere.[188] Similarly, CZTS thin films have been deposited by AACVD on a glass substrate using a toluene solution of $Cu(S_2CNEt_2)_2$, $[Zn(S_2CNEt_2)_2]$ and $[Bu_2Sn(S_2CNEt_2)_2]$ in 2: 1: 1 M ratio.[189] Thin films of CZTS were grown on a glass substrate by spin coating technique using a THF solution of $[(Ph_3P)_2Cu(S_2COEt)]$, $[Zn(S_2CO^nBu)_2]$ and $[Sn(S_2COEt)_2]$ in 2: 1: 1 M ratio and finally heating in a furnace at an appropriate temperature. The films annealed at temperatures <375 °C produced hexagonal phase whereas annealing between 375 and 475 °C produced tetragonal material.[192] Copper zinc tin selenide ($Cu_2ZnSnSe_4$ (CZTSe) has also been prepared by different methods. Hot-injection route using metal salts in an amine (*e.g.*, HDA) and trioctylphosphine selenide (TOPSe) was first reported.[194] Polycrystalline NCs of size 25–30 nm of CZTSe have been prepared

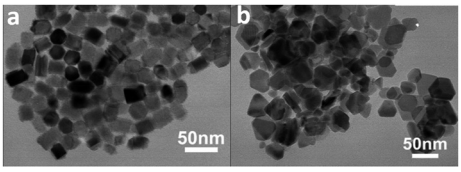

Figure 13: TEM images of wurtzite CZTS a) nano-prisms and b) nanoplates prepared in DDT/OLA and DDT/OA, respectively (reproduced with permission from Royal Society of Chemistry[193]).

by hot-injection method at 280 °C employing $CuCl_2$, $ZnCl_2$, $SnCl_4$ and $(Et_3Si)_2Se$ in ODE and OA mixture.[195] The samples prepared by different routes generally show compositional inhomogeneities.[171] Fuhrmann and coworkers synthesized Cu_2ZnSnE_4 by co-thermolysis of [(tmeda)Zn(μ-E)$_2${$(SnR_2)_2E$}] (R = Me, Bu^t or Ph; E = S or Se) with [{$(Pr^i_3P)Cu$}$_2$$(ECH_2CH_2E)$].[196]

Depending on reaction temperature and the nature of sulfur source, different crystallographic forms can be isolated[197,198] whereas solvent can contribute to the final shape of CZTS nanoparticles.[199] The reaction between metal salts and sulfur powder in an appropriate solvent at high temperatures generally yields nanocrystals of kesterite CZTS.[195] Owing to strong coordinating ability, thiols as a sulfur source, on the other hand, allow the isolation of metastable phases. Thus, the reaction between metal salts and alkanethiols, such as DDT[186,193] or even the thermolysis of metal dithiocarbamate complexes in the presence of thiols (hexadecane thiol)[190] results in the creation of wurtzite CZTS. Thiols also serve as an effective passivating agent for the wurtzite facets and help in decreasing the overall size of the NCs. Another metastable phase–orthorhombic CZTS, could be prepared via hydrothermal method employing stoichiometric quantities of metal chlorides and thiocarbamide dissolved in a mixture of water-ethylenediamine, followed by heating at 200 °C. Orthorhombic CZTS undergoes phase transition on annealing at 500 °C to the tetragonal kesterite structure.[65] The films deposited by thermal degradation of spin-coated CZTS nanoparticles ink gave different CZTS phases depending on the annealing temperature. Annealing at 200 °C produced a mixture of cubic and hexagonal phases, at 350 °C only cubic CZTS phase was formed, while at 500 °C the tetragonal kesterite structure existed.[66]

3.3.2 Synthesis of Cu_2MSnS_4 (M = Mn, Fe, Co, Ni)

There are several protocols to prepare nanocrystals of first-row transition metal ions incorporated compounds, Cu_2MSnS_4 (M = Mn, Fe, Co, Ni). These include hydrothermal/solvothermal,[200–203] hot injection,[204] spray pyrolysis,[205] direct spin-coating or spin-coating of nanoparticles/sol–gel,[206–209] electrodeposition,[210] etc. In these preparative methods stoichiometric quantities of metal salts of copper (CuCl, $CuCl_2{\cdot}2H_2O$, $Cu(NO_3)_2{\cdot}6H_2O$, $Cu(OAc)_2.H_2O$, $Cu(acac)_2$), tin ($SnCl_2{\cdot}2H_2O$, $SnCl_4{\cdot}5H_2O$) and transition metal salts ($MnCl_2{\cdot}4H_2O$, $Mn(OAc)_2.4H_2O$/$FeCl_3{\cdot}6H_2O$, $FeSO_4{\cdot}7H_2O$, Fe(acac)$_2$/$CoCl_2{\cdot}6H_2O$/$NiCl_2{\cdot}2H_2O$, $Ni(NO_3)_2{\cdot}6H_2O$) either as an aqueous solution or in an organic solvent (2-methoxy ethanol, OLA, or organic acids like acetic/citric acid) is treated with a sulfur source like thiourea, Na_2S, $Na_2S_2O_3{\cdot}5H_2O$, elemental sulfur in OLA. Quite often traces of secondary phases (binary and ternary) are also formed. Cui et al.[211] described a general solvothermal method in which a hexylamine solution of CuCl, $SnCl_2$ and MCl_2/$(NO_3)_2$ is treated with a mixture of carbon disulfide and 3-mercaptopropionic acid, followed by heating in an autoclave. The method is employed for the preparation of nanocrystals of these compounds in both zinc blende and wurtzite phases.[211]

Tuneable crystal phases can be prepared by subtle variation in the reaction conditions.[212,213] NCs with the stannite structure of Cu_2CoSnS_4 (band gap 1.58 eV) have been prepared by solvothermal methods,[214,215] while the wurtzite structure could be synthesised by a hot-injection route.[216] On annealing the NCs of wurtzite phase at 400 °C led to the conversion in pure stannite structure. The structure of Cu_2MSnS_4 can also be modified by employing a suitable sulfur source in the reaction. For instance, the use of thiourea as a sulfur source in hydrothermal synthesis of Cu_2MnSnS_4 results in the formation of microspheres of a mixture of hexagonal and tetragonal forms, whereas use of Na_2S in place of thiourea in the reaction afforded fine crystallites of tetragonal phase.[217]

Transition metal incorporated ternary materials show magnetic behaviour. Nanocrystals of Cu_2MnSnS_4 and Cu_2NiSnS_4 display superparamagnetic behaviour at low temperature, whereas NCs of Cu_2FeSnS_4 and Cu_2CoSnS_4 exhibit ferromagnetic behaviour.[211] Cu_2MnSnS_4 (band gap 1.1 eV) shows feeble ferromagnetic behaviour at 2 K.[218]

4 Applications of tin chalcogenides

Binary tin chalcogenides in general find wide array of applications in solar cells, thermoelectric devices, anode material for lithium-ion batteries, etc. due to attributes like suitable band gap range, high optical absorption coefficient (>10^4 cm^{-1}), anharmonicity.[78,83,219] The effectiveness of these applications is further enhanced in 2D layered tin chalcogenides. The basic structure of single-layer tin chalcogenides (SnE) is distinctly different from other layered metal

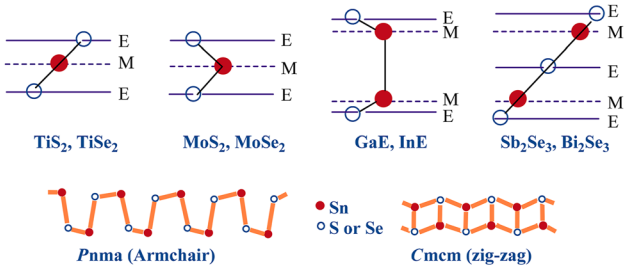

Figure 14: Basic structures of metal chalcogenides (redrawn using data from[220] (Taylor & Francis) and[219] (MDPI).

chalcogenides and comprises armchair and zig-zag arrangement of tin and chalcogen atoms (Figure 14).[219,220]

In general application of a semiconducting material depends on its physicochemical, optical and electronic properties as well as size, shape, composition, crystal and band structures, etc. which in turn is governed by synthetic routes and post-synthetic surface modifications. Among various synthetic approaches described earlier, exfoliation of material in top-down approach can be utilized for the preparation of 2D layered materials which can be used for thermoelectric devices while the 2D nanostructured thin films deposited by using SSMPs can be utilized for photovoltaic applications. The bottom-up approach relying on solution phase/colloidal synthesis of nanomaterials provides a good control over the morphology (0D, 1D, 2D and 3D, etc.), phase and composition. Accordingly, these materials can be employed for different applications. For instance, 0D materials, especially quantum dots (QDs) are preferable for bio-imaging[221] and dye degradation[222] while 1D nanowires, nanorods are better choice for field effect transistor (FET),[78,223] sensors[78] and photovoltaic,[224] etc. applications. Solvothermal synthesized 1D SnS nano-rods show outstanding emission properties viz. low turn-on field (2.5 V/μm for 10 μA/cm^2), high emission current density (647 μA/cm^2 at 3.9 V/μm) and superior current stability (5 h for ~ 1 μA).[223] On the other hand, 2D materials where the charge carriers are quantum confined along their thickness and having a large dielectric contrast produce large exciton binding energies leading to exceptional optical and electronic properties.

4.1 Photovoltaic solar cells

Silicon-based solar cells currently command photovoltaic energy generation with ~95 % market share (https://www.energy.gov>eere>solar-photovotaic-cell). To overcome the inherent drawbacks of silicon, thin film-based PV devices fabricated from direct band semiconductor materials like CdTe, $CuInE_2$ (E = S or Se) gained traction.[225] Scarce abundance of In, Te and toxicity of cadmium, however, limit their large-scale PV utilization. Tin chalcogenides (binary, ternary, quaternary materials) are well-suited for PV applications[39,53] as they fulfil the following criteria expected from an ideal material for PV applications.[226]

- Direct-band semiconductor with band-gap of 1.1–1.7 eV.
- High photovoltaic conversion efficiency.
- Easily accessible constituent elements with low or nearly no toxicity.

Binary tin chalcogenides SnS and SnSe have an ideal bandgap energy (~1.3 eV), high absorbance coefficient (>10^{-4} and >10^{-5} cm^{-1}) and high carrier concentrations (10^{15}–10^{18} cm^{-3}) making them promising candidates as absorber material for PV solar cells. Their thin layers (~300 nm thick) can absorb most of the useful solar spectrum. Theoretically predicted maximum power conversion efficiency (PCE) is 32 % for SnE-based single junction thin film solar cells.[227] A number of groups have fabricated PV devices based on SnE thin films deposited by a variety of methods and reported PCE of 0.1–6.4 % depending on the structure of SnE and solar cell configuration.[83,228,229] Ahmet et al. fabricated solar cells using α-SnS and π-SnS thin films with two different configurations – Mo/SnS/CdS/i-ZnO/ITO and FTO/SnS/CdS/i-ZnO/ITO and demonstrated that the α-SnS based devices performed better with PCEs of 0.82 and 0.88 % than the π-SnS thin film-based devices with PCEs of 0.21 and 0.15 %, respectively.[228] Elongated anisotropic NCs (19.0 ± 5.1 nm) of orthorhombic SnSe, prepared from anhydrous $SnCl_2$ and $Bu^t_2Se_2$ in a mixture of dodecyl amine and dodecane thiol (5:1 v/v ratio) at 180 °C, exhibit photovoltaic properties.[224] The orthorhombic SnSe films, deposited from [Bu^t_2Sn(Sepy)$_2$] on glass and p-type silicon(100) substrates at 490 °C, in Si/SnSe/Au configuration showed photo-response with a bias of 1.5 V. There was-20 % increase in the current under illumination conditions (Figure 15).[123] Similarly nanosheets of $SnSe_2$, obtained from [Bu^t_2Sn(SepyMe-5)$_2$], show photo response and the photocurrent increased under illumination.[126]

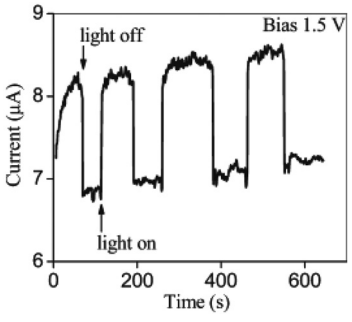

Figure 15: Photo-response of the SnSe thin film deposited on a silicon substrate by the AACVD of [Bu^t_2Sn(Sepy)$_2$] at 490 °C with a bias voltage of 1.5 V (reproduced from Royal Society of Chemistry.[123]

Owing to the anisotropic structure, SnE (E = S or Se) show a reckonable difference in their optical and electrical properties along different crystallographic directions. For instance, electrical conductivity of SnS nano-sheets differ significantly in two different anisotropic crystalline directions.[230] The geometry-controlled SnE nanosheets have been projected for their high-efficiency photonics and electronics applications.[230] Furthermore, 2D nanosheets of SnS[231] and SnSe[232] have also been employed as absorbing layers of solar cells with photoelectric conversion efficiency of 1.45 and 4.8 %, respectively.

Ternary and quaternary compounds have also been investigated for their photovoltaic solar cell applications. Cu_2SnS_3 and Cu_2SnSe_3 are isostructural and their NCs have an attractive potential for making low-cost thin-film-based solar cells due to their solution processability. The status of CTS for solar cell applications has been reviewed.[233,234] A general schematic configuration of solar cells is illustrated in Figure 16. Tetragonal Cu_2SnS_3 thin-films based solar cells have been designed with graphite/Cu_2SnS_3/ZnO/ITO/SLG configuration. The cells showed PCE of 2.1 % with open circuit voltage.[235] Recently it has been shown that the solar cell constructed using NCs of wurtzite-CTS showed much better (13.1 % PCE) photovoltaic performance in comparison to the zinc blende phase (7.87 % PCE).[236]

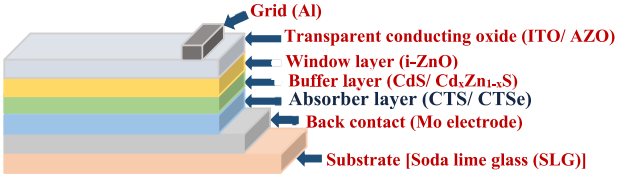

Figure 16: A general schematic configuration of Cu_2SnE_3 solar cells.

Nanostructures of Cu_2SnE_3 (E = S or Se), prepared by using organometallic precursors, exhibit photo response in a photo-electrochemical cell.[127,128] Photo-response of nanostructures (CTS, SnS and $Cu_{1-8}S$) has been assessed. A nonlinear current voltage (I–V) behaviour of their nanostructures has been noted. CTS nanostructures exhibited better photosensitivity as well as increased photo-response over several on-off cycles with faster switching characteristics as compared to $Cu_{1-8}S$ particles.[128] The nano-structures of Cu_2SnSe_3 in a photo-electrochemical cell (Figure 17) exhibited a PCE of 1.7 %.[127]

The energy band gap of CZTS (~1.5 eV) exists in the visible region and can be further tuned by changing the composition, phase and size of the NCs. For example, the band gap of the wurtzite phase of $Cu_2ZnSn(S_{1-x},Se_x)_4$ can gradually be tuned from 1.4 eV (for x = 0) to 0.9 eV (for x = 0.8) (Figure 18).[237] The CZTS band gap can be altered from 1.5 to 1.8 eV by reducing NCs size from 7 to 2 nm–a regime (~3 nm) where quantum confinement effect can be noted.[1]

Tuneable band gaps lying in the visible region and excellent light absorption coefficients of these materials are apt for photovoltaic applications. The early investigations on CZTS-based solar cells reported 6.7 % photoelectric conversion efficiency[12] which with successive improvements in preparation of materials with different solar cell device structures[238–241] have reached ~11 %.[241] Further improvement in photoelectric conversion efficiency (12.6 %)[242] is reported on selenization, $Cu_2ZnSn(SSe)_4$. There is a huge difference between the experimentally observed and theoretically predicted (31.6 %) PCEs.[227] A number of factors have been attributed for the large gap in

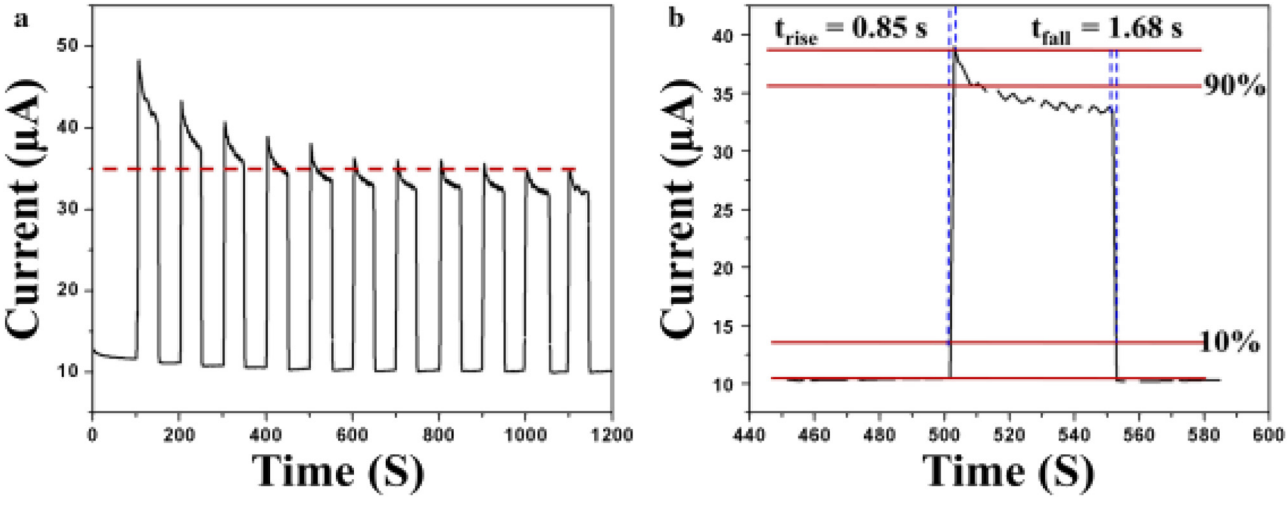

Figure 17: Current vs time plot of CTSe nanostructures obtained by thermolysis of [$Me_2Sn(2\text{-}SeC_5H_3(Me\text{-}3)N)_2$] and [$Cu\{SeC_5H_3(Me\text{-}3)N\}]_4$ in OLA at 300 °C by heat up method showing switching behaviour under light intensity of 200 μW/cm^2; b expanded view of one of the cycle. (Reproduced with permission from Springer Nature Publishers.[127]

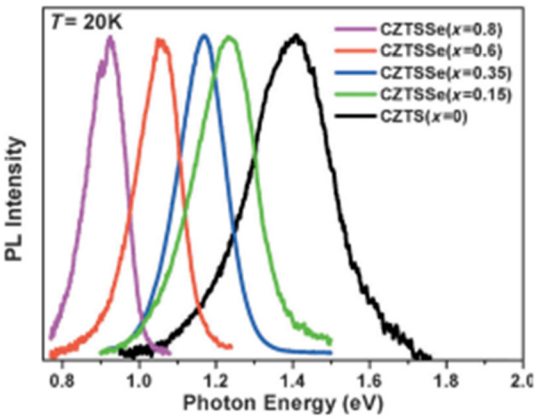

Figure 18: Photoluminescence (PL) emission of $Cu_2ZnSn(S_{1-x},Se_x)_4$ nanocrystals. (Reproduced with permission from Wiley.[237]

Table 3: Electrical properties of different phases of CZTS (data from[192]).

	Hexagonal material (wurtzite phase)	Tetragonal (kesterite phase)
Resistivity (Ω cm)	27.1	1.23
Carrier concentration (cm^{-3})	2.65×10^{15}	4.55×10^{17}
Hall mobility (μ) ($cm^2\ V^{-1}\ s^{-1}$)	87.1	11.1
Hall coefficients (R_H) ($C^{-1}\ cm^3$)	2.36×10^3	13.7
Conductivity (σ) ($S\ cm^{-1}$)	0.0369	0.81

power conversion efficiencies. These include structural defects in the CZTS absorber, presence of different phases, which is often the case, each having different electrical properties (Table 3),[192] presence of secondary materials.

Cu_2MSnS_4 (M = Mn, Fe, Co, Ni) based on earth-abundant elements have also been explored as an alternate material for low-cost solar cells. They are p-type direct-band semiconductor materials with an energy band gap of 1.21–1.69 eV and exhibit good photostability with desirable optical absorption coefficient ($>10^4\ cm^{-1}$).[206–210] Photovoltaic devices with $Mo/Cu_2MnSnS_4/CdS/TCO/top$ and $SLG/Cu_2CoSnS_4/Al$ geometry were fabricated and evaluated for their power conversion efficiencies.[209,210] The PCE of the former device was 0.19 % which increased to 0.73 % on sodium doping.[243] The $SLG/Cu_2CoSnS_4/Al$ photodetector exhibited current amplification by an order of magnitude from dark to solar lamp and 1,064 nm IR laser illuminations.[209]

4.2 Dye sensitized solar cells

Dye sensitized solar cells (DSSC) is another approach to utilize solar energy. A typical configuration of a DSSC is a transparent conductive glass substrate, a sensitizer adsorbed photoanode (usually TiO_2 nanoparticles), platinum as a counter electrode (CE) which are placed in a redox electrolyte solution such as I^-/I_3^-, S^{2-}/S_x^{2-}, etc. There have been sustained efforts to enhance the performance of DSSCs; replacement of platinum as CE is one of the strategies among various other components of the cell.[244] Numerous metal chalcogenides have been explored due to their rich intercalation chemistry and electronic properties.

Tin chalcogenides have also been explored as an absorber material in DSSCs. Binary chalcogenides, SnS_2, $SnSe_2$ and SnSe have been examined as counter electrodes in a DSSC.[245–247] Reduced graphene oxide composite of SnS_2 nanoparticles (SnS_2@rGO) as CE exhibited a PCE of 7.12 % in DSSC. The PCE of SnS_2@rGO is comparable to platinum CE (6.79 %), but much better than either SnS_2 nanoparticles (5.58 %) or graphene sheet alone (3.73 %).[247] Screen-printed SnSe and platinum counter electrodes exhibited PCEs of ~5.76 % and 8.09 % with open-circuit voltages of 0.63 and 0.68 V, respectively in DSSC containing iodide/triiodide redox couple.[245] Hierarchical nanostructures (HNs) of SnSe and $SnSe_2$ obtained in a solvothermal method has been used as counter electrodes in a dye sensitized solar cell which demonstrated photovoltaic performances similar to the device fabricated with a traditional platinum counter electrode.[246] A PCE of 5.60 % is realized when $SnSe_2$ HNs were employed as the counter electrode of DSSC which is nearly equal to the efficiency noted for a conventional Pt counter electrode (5.74 %). $SnSe_2$ QDs deposited on TiO_2 nanocrystalline porous films show PCE of 0.12 % under AM 1.5, 1 sun, which is much higher than the bare TiO_2 electrode (PCE = 0.004 %).[248]

The photovoltaic properties of quaternary tin chalcogenides, besides their applications in thin film solar cells, are being exploited in DSSCs as low-cost replacement of conventional noble metal-based counter electrode (CE) materials. Thin films prepared from CZTS nanocrystals emerged as effective counter electrode material in DSSCs.[249–251] Thin films of CZTS grown on FTO glass by spin coating using a toluene dispersion of CZTS nanocrystals (15 ± 6 nm) followed by annealing either in the presence or absence of selenium vapours at 540 °C have been evaluated for their DSCCs applications. The selenized films showed higher PCE of 7.37 % as compared to CZTS (3.62 %) and also from conventionally used platinum electrodes (7.04 %).[250] 2-D wurtzite CZTS nanosheets of ~30–50 nm thickness, when used as CE catalyst for DSSCs, exhibit superior power conversion efficiency of 6.68 % than that of 0-D CZTS nanospheres (5.58 %), but similar to Pt counter electrode.[251]

4.3 Photocatalysts

4.3.1 Photo-electrocatalysts for water splitting

Photo-electrochemical hydrogen evolution reaction (HER) for generation of hydrogen by splitting of water is another

important reaction where layered metal chalcogenides have been explored as catalysts. HER involving post transition metal chalcogenides has been reviewed recently.[7] HER is a two-step process. It involves the reduction of proton and desorption of H_2 molecules from the electrode surface. Both mono and dichalcogenides of tin, SnE and SnE_2 (E = S or Se) have been examined as catalysts for HER.[7] Density functional theory (DFT) calculations have revealed that SnS_2 indicated stronger HER electrocatalytic behaviour than SnS.[252]

Water splitting by single-layers of SnS_2 deposited on indium-tin-oxide (ITO) coated glass has been investigated by photoelectrochemical (PEC) measurements in a 0.5 M Na_2SO_4 electrolyte using a three-electrode setup.[253] The single-layers of SnS_2 could produce photocurrent density up to 2.75 mA cm^{-2} at 1.0 V versus Ag/AgCl, which is 70 times higher than the bulk material. They showed conversion efficiency of 38.7 % under visible light. Lattice mismatched layered SnS_2/SnS superstructures show photocatalytic activity for H_2 generation under blue light (450 nm) irradiation with H_2 evolution rates of ~ 100 µmol h^{-1}, but there was negligible evolution of H_2 under green light (500 nm) irradiation.[254] Orthorhombic SnSe/FTO films, grown from [$Bu_2Sn(SeCOPh)_2$], show photoelectrochemical (PEC) behaviour. The films show bifunctional behaviour, *i.e.,* can be utilized for both HER and oxygen evolution reaction (OER) by swapping the applied potential.[135] At 0 V, hydrogen evolution was noted but at 0.1 V the electrode switched to OER.[135]

4.3.2 Photocatalytic activity

Binary, ternary and quaternary tin chalcogenides show photocatalytic activity under solar irradiation. A typical photocatalysis mechanism for binary metal chalcogenides is shown in Figure 19. SnS quantum dots (2.5–3.0 nm size), produced by co-precipitation method using $SnCl_2{\cdot}2H_2O$ and thiourea in ethylene glycol, act as a catalyst for photo-degradation of eosin yellow and brilliant green dyes under sunlight.[222] Superoxide ions formed during solar illumination are responsible for photodegradation of these dyes.

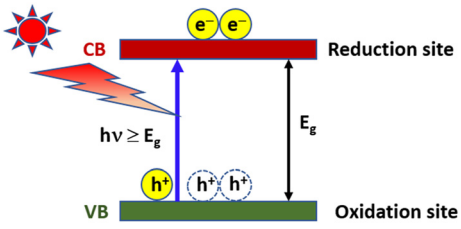

Figure 19: Photocatalysis mechanism for binary metal chalcogenides.

Visible-light-driven photocatalytic activity of Cu_2SnE_3 compounds has been investigated in photo-degradation of organic dyes.[163,255,256] Nanosheets of Cu_2SnS_3 (band gap ~ 2.42 eV)[163] and nanoflakes of Cu_2SnSe_3 (band gap ~1.14 eV)[256] with rough surfaces show photo-catalytic activity in photo-degradation reaction of methylene blue (MB). The latter could degrade 73 % of the MB dye in 3 h of light irradiation. The Cu_2SnS_3@rGO (3 %) nanocomposite unveils superior photocatalytic activity than that of pure Cu_2SnS_3 in photo-degradation of eosin under visible-light.[255] The improved photocatalytic activity of Cu_2SnS_3@rGO has been ascribed to the creation of distinct interface between constituents of the composite facilitating charge carrier separation in the Cu_2SnS_3.

The photocatalytic activity of CZTS has also been investigated through dye degradation and hydrogen evolution reaction.[257] CZTS exhibited photocatalytic activity through photodegradation of Congo red azo dye[184] and RhB[258] under simulated solar irradiation. The catalyst could degrade 90.2 % Congo red azo dye in just 60 min and could also be reused repeatedly for dye degradation.[201]

Nano-crystals of Cu_2MSnS_4 (M = Fe or Co), synthesized by hydrothermal route, exhibited photocatalytic activity, NCs with rough surfaces being more active.[201,256] The Cu_2FeSnS_4 nanoflakes could degrade almost 74 % of methyl red dye within 3 h of light illumination,[256] whereas the nanocrystals of Cu_2CoSnS_4 (size 26–40 nm) photo-catalytically degraded methylene blue dye (78 %) and crystal violet dye (84 %).[201]

4.4 Thermoelectric properties

Thermoelectric (TE) materials interconvert heat and electricity. They are used in solid state cooling and power generating devices. A thermoelectric device based on Seebeck effect is depicted in Figure 20. Thermoelectric gradient developed between hot and cold junctions results in carrier gradient which in turn develops electrostatic potential in the circuit. There have been unrelenting

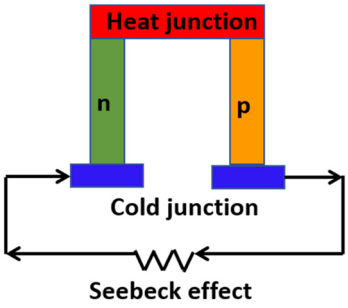

Figure 20: A typical thermoelectric device based on Seebeck effect.

efforts to enhance the value of figure of merit (ZT) to improve thermoelectric performance of the TE devices. The ZT value of commonly used commercial materials (*e.g.,* PbTe, Bi_2Te_3) is ~1.[2,259] ZT can be calculated by using the formula, $ZT = S^2\sigma T/\kappa$, where S, σ, T, and κ denote the Seebeck coefficient, electrical conductivity, absolute temperature, and thermal conductivity. A dramatic enhancement of ZT value in dimensionally confined thermoelectric materials has been observed.[2,259,260] Accordingly, several anisotropic metal chalcogenides nanocrystals, including tin, have been extensively examined as thermoelectric materials in the past few decades.

Tin monochalcogenides, particularly tin selenide and tin telluride, are known to be narrow band gap semiconductors with their bulk band gap falling in the range of 0.21–1.3 eV. The latter property makes them reasonably good conductors above the room temperature while an interplay of structurally driven anisotropy, temperature-induced phonon softening and many body phonon scattering results in lowering thermal conductivity in these materials. Both these factors make them good thermoelectric materials with a rational ZT value and have emerged as promising thermoelectric materials for low- and moderate-temperature range TE devices. Accordingly, both metal doped and undoped tin monochalcogenides have been studied by a number of workers. SnE (E = S, Se or Te) nano-powders produced by solvothermal method have been evaluated for thermoelectric applications. SnS and SnSe unveiled extraordinary anisotropy in both electrical and thermal properties which may be ascribed to their layered crystal structure. SnS, SnSe and SnTe samples exhibited ZT values of 0.13 at 773 K, 0.21 at 773 K and 0.79 at 873 K, respectively with the highest ZT value for SnTe.[88] As-grown 2-D SnS crystals show heavily hole-doped (~10^{19} cm^{-3}) conductivity and strong in-plane anisotropy. Mobility along the zigzag direction (20 $cm^2 V^{-1} s^{-1}$) is 1.7-fold higher as compared to armchair direction,[261] whereas the monolayers of SnS show higher carrier mobility (10,000 to 38,000 $cm^2 V^{-1} s^{-1}$) along the '*a*' direction.[262] The monolayers of SnS also show higher degree of thermal anisotropy and exhibit a high ZT in different directions.[263]

Kanatzidis and co-workers demonstrated that bulk SnSe, a *p*-type thermoelectric material, has the highest ZT value 2.6 ± 0.3 at 923 K along the *b* axis but exhibits lower values of 2.3 ± 0.3 and 0.8 ± 0.2 along the *c* and *a* axis, respectively. The high ZT value along the *b*-axis has been ascribed to very low lattice thermal conductivity in SnSe.[40,264] In fact, SnSe has an ultralow value of *K* for *Cmcm* phase and at above 800 K its value is ~0.25 $W m^{-1}K^{-1}$ which is even significantly lower than p-type PbTe.[264] Using sodium as an acceptor in hole-doped SnSe single crystals, delivered a peak *ZT* of 2.0 at 773 K.[265] SnSe/reduced graphene oxide nanocomposites with rGO: 0.1, 0.3, 0.5, 0.7 wt%, have been prepared which showed substantial drop in the lattice thermal conductivity with the highest ZT value of 0.91 for the sample containing 0.3 % rGO.[266] Bismuth-doped SnSe single crystals act like n-type semiconductor with enhanced carrier concentration and results in improved ZT value of 2.2 along *b* axis at 733 K, but along *c* and *a* axes the ZT values are 2.1 and 0.8, respectively.[267] Surface-treated nanocomposites of SnSe–CdSe with large number of defects demonstrated one of the best reported ZT values of 2.2 at 786 K, for solution-processed SnSe.[268] Thermoelectric properties of SnTe NCs with different dopants have been investigated. A significant enhancement in the ZT value of indium-doped SnTe has been reported which reached ~1.1 at 873 K in 0.25 atom % In-doped SnTe while ZT value for undoped SnTe is ~0.7 at about 873 K.[269] SnTe nanosheets consisting of ~3 nm size nanoparticles show *ZT* of ~1.1 at 923 K without any dopant and exhibited considerable reduction in the lattice thermal conductivity.[270]

Cu-IV-VI compounds also exhibit thermoelectric (TE) properties and thus find applications in thermoelectric devices. The monoclinic CTS exhibits low ZT ~0.05 above 700 K owing to its low carrier concentration and high thermal conductivity. However, to enhance the carrier concentration and reduce the thermal conductivity, materials with external doping by various metal ions at the Sn site have been explored. Such doping results in phase transformation from monoclinic to cubic phase with concomitant increase in ZT value to ~0.4–0.8 above 700 K.[271] For example, silver doped CTS [$Cu_2Ag_{(x)}Sn_{(1-x)}S_3$ ($0.05 \le x \le 0.25$)] showed a power factor an order greater than the undoped CTS. The silver doped samples exhibited the highest zT ~ 0.8 at 723 K.[272]

Similarly, Cu_2SnSe_3 shows excellent thermoelectric properties.[165,273] It is a direct band gap (0.84 eV) p-type semiconductor and adopts a 3D distorted diamond-like structure. It has a high absorption coefficient (>10^4 cm^{-1}) and comparatively high hole mobilities (870 $cm^2 V^{-1} s^{-1}$).[274,275] Monoclinic Cu_2SnSe_3, prepared by heating constituent elements at 850 K, showed the thermoelectric figure of merit ZT of 0.33 at 650 K.[175] Efforts have been made to lower the thermal conductivity by reducing the crystal domain dimensions of Cu_2SnSe_3 to the nano regime.[165] Partial substitution of Sn atoms by Co, in Co:Cu_2SnSe_3 nanostructure, led to the enhancement of electrical conductivity and resulted in ZT up to 0.63 at 715 K.[276]

Relatively high thermoelectric properties of quaternary materials which originate from low thermal conductivities of these materials have made them attractive candidates for high temperature thermoelectric applications.[175,277,278] A variety of off-stoichiometric materials were developed to optimize the thermoelectric properties. The ZT value of 0.91 at 860 K for $Cu_2ZnSnSe_4$ films is appropriate for high

temperature applications. Cu_2NiSnS_4 nanoparticles show interesting thermoelectric properties.[278]

4.5 Lithium- and sodium-ion batteries

Graphite has reversible capacity of 372 mA h g^{-1}. It is the most commonly used anode material in rechargeable Li-ion batteries (LIBs) despite its inability to meet the energy density of high-power LIBs. Therefore, alternate materials such as metals and metal oxides, layered metal sulfides and selenides have been explored.[22]

Tin chalcogenides, due to their layered-structures, have also been investigated for lithium-ion batteries (LIBs) and sodium-ion batteries (SIBs) as anode material. Applications of SnS_x materials in LIBs and SIBs have been reviewed by Pang and co-workers.[279] Tin sulfides, SnS and SnS_2 are layered semiconductors with the inter-layer separation of 0.43 and 0.59 nm, respectively. The maximum theoretical reversible capacities of SnS and SnS_2 are 792 and 645 mA h g^{-1}, respectively for LIB anodes.[280,281] Their inter-layer spacing facilitates entry of both Li^+ and Na^+ ions in the crystal lattice of tin sulfides. However, due to rapid structure deterioration and low-capacity retention, use of these materials is rather limited.[22] For example, electrode based on hexagonal nanosheets of SnS_2, prepared by hydrothermal route employing $SnCl_4{\cdot}5H_2O$ and thioacetamide, exhibited high discharge capacity of 513 mAh g^{-1} after 50 cycles with 96 % retention in Li-ion battery, whereas electrode made by using SnS_2 powder deteriorated quickly after several cycles due to pulverization. The discharge capacity was also much higher than that of carbon electrodes.[282] Coin type electrochemical cell fabricated from $SnSe_2$ nanoplates-graphene composite exhibited superior storage capacity (first discharge capacity 1,400–1730 mA h g^{-1} and reversible capacity at 30th cycle 470–640 mA h g^{-1}) than those made from either reduced graphene oxide (315 mAh g^{-1}) or $SnSe_2$ nanosheets (420 mAh g^{-1} first 10 cycles and reduced to 260 mAh g^{-1} at the 30th cycle).[283]

Nanosheets of SnS, obtained by thermolysis of $[Bu^t_2Sn(Spy)_2]$, have been evaluated as anode material for LIBs in half-cell configuration.[129] A cycle test has been performed in the voltage range 0.1–0.3 V. The charge and discharge capacities of the first cycle are 1,306 and 958 mA h g^{-1} respectively at 50 mA g^{-1} current density. The electrode could be recycled for 50 cycles (Figure 21).[129] Performance of orthorhombic SnSe nanosheets synthesized by thermolysis of $[Me_2Sn\{2\text{-}SeC_5H_2(Me\text{-}4,6)_2N\}_2]$ has been evaluated as an anode material in LIBs. These nanosheets show an initial specific capacity of 1,134 mA h g^{-1} at 50 mA g^{-1} and hold a capacity of 380 mA h g^{-1} at the end of 70 cycles with 100 % efficiency.[121] Similarly, SnSe nanonetworks have been evaluated as LIB anode material which presented a discharge capacity of 1,000 mAh g^{-1} at a current of 100 mA g^{-1} for 50 cycles and a retention capacity of 92 %.[284]

Ternary tin chalcogenide-based nanomaterials have also been examined for LIB anode materials.[285] Wu et al. probed the Cu_2SnS_3 polycrystalline nanoparticles as an excellent electrode for LIBs.[286] The large interlayer separation (2.280 Å) and tunnel size ($3.921 \times 5.587 \times 4.210$ $Å^3$) in the Cu_2SnS_3 structure, which is significantly larger than the diameter of the lithium ions (1.36 Å), would facilitate diffusion of lithium ions through the crystal structure.[286] Different nanostructures of Cu_2SnS_3 including mesoporous spheres,[287,288] hollow microsphere,[289] small nanoparticles,[290] cabbage-like nanostructures[291] have been investigated as anode materials for LIBs. Cabbage-like nanostructures of Cu_2SnS_3 showed excellent stability and high reversible capacity of 621 mA h g^{-1} after 50 cycles.[291]

$ZnSnS_3$@rGO nanocomposite exhibited large specific capacity and high-rate capability in lithium- and sodium-ion-storage devices. It delivered a capacity of 472.2 mAh g^{-1} at 100 mA g^{-1} and hold a specific capacity of 401.2 mAh g^{-1} after 200 cycles in Na-ion cells whereas in Li-ion cells, it showed capacity of 959.2 mAh g^{-1} at a current density of 100 mA g^{-1} and sustained a specific capacity of 551.3 mAh g^{-1} at a high current density of 1 A g^{-1} upon 500 cycles.[179]

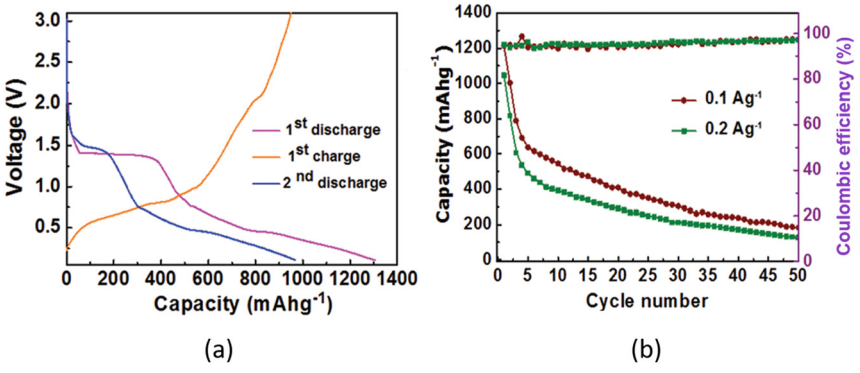

Figure 21: (a) Charging–discharging voltage profile at 50 mA g^{-1} current density, (b) performance of SnS with the number of cycling. (Reproduced from Royal Society of Chemistry.[129]

CZTS and its derivatives have been explored as electrode materials for LIBs. As prepared CZTS microstructures have also been used for LIBs anode materials. These electrodes delivered a first discharge specific capacity as high as 1,125 mA h/g which remained at 786 mA h/g after 100 cycles.[292] Carbon-coated CZTS nanoflowers with a 3D architecture have been developed as high-performance anode materials which showed high gravimetric (1,366 mA h/g) and areal (2.45 mA h/cm^2) capacities.[6] Cu_2CoSnS_4 has been shown to be an excellent anode material for rechargeable LIBs.[293] It exhibits an average specific capacity of 198.7 mA h g^{-1} at a current density of 0.1 A g^{-1}.

4.6 Supercapacitors

Supercapacitors are electrochemical high-capacity energy storage devices. They exhibit high power density, rapid charging/discharging efficiency and long cyclic stability and are considered as replacement of Li-ion batteries. Suitable Faradic behaviour and layered structure of SnS_2 has made this as a promising electrode material for supercapacitors.[294] Nanocomposites tin sulfide (SnS_2) nanoflakes anchored on polyaniline nanofiber network deposited on graphite foam (GF), SnS_2@PANi@GF, exhibit high specific capacitance (365 F g^{-1} at 10 mV s^{-1}) and long cycle durability of 5,000 cycles with a retention capacity of 73 %.[295]

Cu_2MSnS_4 finds applications as high energy density supercapacitors.[200,202,296,297] As-fabricated device containing Cu_2MnSnS_4 electrode material showed an energy and power densities of 27 W h kg^{-1} and 759 W kg^{-1}, respectively at a current density of 1 A g^{-1} and retained 80.35 % capacity with 97.54 % Coulombic efficiency after 21,000 cycles.[297] The iron-based device Cu_2FeSnS_4/PVP/rGO provided 86.40 % capacity retention after 5,000 cycles,[200] the nickel-based Cu_2NiSnS_4 retained 95.7 % of its initial capacitance after 2000 charge-discharge cycles.[202]

4.7 Sensor materials

Tin sulfides have also been used as sensor material. SnS_2 nanoflakes show high sensitivity and superior selectivity in sensing NO_2 at less than 160 °C.[298] Sensors fabricated using SnS_2 with nanoscale defects show ultra-high sensitivity of 2.5 ppb for NO_2 at room temperature.[299] Two-dimensional SnS has also been used for NO_2 sensing.[300] The device could sense NO_2 down to 3.75 ppm. SnS nanoflakes have been employed in sensors for detection of methanol, ethanol, acetone and 1-butanol.[301] The device showed excellent sensing properties for acetone with a maximum response of 1,000 % at 100 °C and rise and fall times of 3 and 14 s, respectively.

4.8 Future development

The outlook of materials lies in the development of ecologically benign, earth-abundant, and sophisticated yet robust materials for various advanced technologies. A step in this direction is the development of advanced tin chalcogenides such as self-assembled or ordered NC assemblies for innovative and cutting-edge technologies. To realize the potential of these materials, evolution of scalable methods for superior quality materials are highly warranted. One of such methods is single source molecular precursor (SSMP). A vigilant attention towards designing these precursors through proper selection of ligands can customize the precursors with specific reactivity to produce targeted materials with explicit shape and stoichiometry. For instance, nature of ligands can control the volatility of the precursors, coordination environment around the metal in metal complexes, labile nature of C-E (E = S, Se or Te) bond (in case of metal derivatives of chalcogen ligands) which in turn govern the decomposition of SSMP and hence the quality of the final product. In addition to the above, reaction conditions such as solvent nature, temperature, time impact the size, shape, stoichiometry, crystallinity, and crystal structure of the resulting product and hence their properties. In depth study of all the factors affecting the quality and properties of the desired material could launch sturdy synthesis protocols for binary-, multinary- and ordered-tin chalcogenides. At current juncture, quite a few molecular precursors for tin-sulfides and -selenides have been established while meagre precursors exist for tin tellurides and multinary-tin chalcogenides.

5 Conclusions

From the foregoing account it is evident that versatile electronic properties, semiconducting behaviour, high thermoelectric performance, and benign nature of tin chalcogenides make them frontrunner among main group chalcogenides for a variety of applications. The scope and horizon of their utility can be further expanded by modulating their size, shape, morphology and even the number of layers in the material. Single source molecular precursor route has quite conveniently employed in altering and controlling the properties of chalcogenide materials as demonstrated for binary systems. Such precursors for ternary and quaternary systems are scanty. Design and development on single source molecular

precursors for ternary and quaternary systems may permit synthesis of phase pure and desired structure of materials under moderate reaction conditions. Although the quaternary systems exhibit promising photovoltaic and thermoelectric properties, their long-term stability in devices are yet to be ascertained. Intercalation of guest atoms in the layers of semiconducting binary tin chalcogenides would provide new properties for further exploitation. Clearly tin chalcogenides offer several opportunities and new possibilities in different areas of basic research and technology. It is hoped that this review would accelerate further growth of tin chalcogenides and would assist in realizing their utility in different areas.

Acknowledgments: We thank the Department of Atomic Energy for sustained funding. The contributions of our collaborators, colleagues, and students whose names appear as co-authors in the publications are gratefully acknowledged.
Research ethics: Not applicable.
Informed consent: Consent is obtained from the coauthor who has equally contributed in the preparation of this review article.
Author contributions: All authors have accepted responsibility for the entire content of this manuscript and approved its submission.
Use of Large Language Models, AI and Machine Learning Tools: None declared.
Conflict of interest: The authors state no conflict of interest.
Research funding: None declared.
Data availability: Not applicable.

References

1. Khare, A.; Wills, A. W.; Ammerman, L. M.; Norris, D. J.; Aydil, E. S. *Chem. Commun.* **2011**, *47*, 11721–11723.
2. Kanatzidis, M. G. *Chem. Mater.* **2010**, *22* (3), 648–659.
3. Phalswal, P.; Dey, A.; Khanna, P. K. *Mater. Chem. Phys.* **2024**, *319*, 129264.
4. N'guessan, A. I.; Bouich, A.; Soro, D.; Soucase, B. M. *Heliyon* **2023**, *9* (8), e19057.
5. Scarpulla, M. A.; McCandless, B.; Phillips, A. B.; Yan, Y.; Heben, M. J.; Wolden, C.; Xiong, G.; Metzger, W. K.; Mao, D.; Krasikov, D.; Sankin, I.; Grover, S.; Munshi, A.; Sampath, W.; Sites, J.; Bothwell, A.; Albin, D.; Reese, M. O.; Romeo, A.; Nardone, M.; Klie, R.; Walls, J. M.; Fiducia, T.; Abbas, A.; Hayes, S. M. *Sol. Energy Mater. Sol. Cell.* **2023**, *255*, 112289.
6. Venugopal, B.; Syum, Z.; Yu, S.-Y.; Sabbah, A.; Shown, I.; Chu, C.-W.; Chen, L.-C.; Lee, C.-H.; Wu, H.-L.; Chen, K.-H. *ACS Omega* **2022**, *7* (11), 9152–9163.
7. Wang, Y.; Zhao, Y.; Ding, X.; Qiao, L. *J. Energy Chem.* **2021**, *60*, 451–479.
8. Mohammad, N.; Khanna, P. K. *Hybrid. Adv.* **2024**, *5*, 100169.
9. Yadav, A. K.; Mohammad, N.; Khanna, P. K. *Mater. Adv.* **2023**, *4*, 4409.
10. Yadav, A. K.; Mohammad, N.; Chamanehpour, E.; Mishra, Y. K.; Khanna, P. K. *RSC Appl. Polym.* **2024**, *2*, 775.
11. Mohammad, N.; Khanna, D.; Phalswal, P.; Khanna, P. K. *Mater. Lett.* **2023**, *347*, 134597.
12. Katagiri, H.; Jimbo, K.; Maw, W. S.; Oishi, K.; Yamazaki, M.; Araki, H.; Takeuchi, A. *Thin Solid Films* **2009**, *517* (7), 2455–2460.
13. Brus, L. E. *J. Phys. Chem.* **1984**, *80*, 4403–4409.
14. Efros, A. L.; Brus, L. E. *ACS Nano* **2021**, *15* (4), 6192–6210.
15. Geim, A. K.; Novoselov, K. S. *Nat. Mater.* **2007**, *6*, 183–191.
16. Novoselov, K. S.; Geim, A. K.; Morozov, S. V.; Jiang, D.; Zhang, Y.; Dubonos, S. V.; Grigorieva, I. V.; Firsov, A. A. *Science* **2004**, *306*, 666–669.
17. Chhowalla, M.; Shin, H. S.; Eda, G.; Li, L.-J.; Loh, K. P.; Zhang, H. *Nat. Chem.* **2013**, *5*, 263–275.
18. Chhowalla, M.; Liu, Z.; Zhang, H. *Chem. Soc. Rev.* **2015**, *44*, 2584–2586.
19. Miro, P.; Audiffred, M.; Heine, T. *Chem. Soc. Rev.* **2014**, *43*, 6537–6554.
20. Voiry, D.; Mohite, A.; Chhowalla, M. *Chem. Soc. Rev.* **2015**, *44*, 2702–2712.
21. Duan, X.; Wang, C.; Pan, A.; Yu, R.; Duan, X. *Chem. Soc. Rev.* **2015**, *44*, 8859–8876.
22. Giri, A.; Park, G.; Jeong, U. *Chem. Rev.* **2023**, *123* (7), 3329–3442.
23. Heine, T. *Acc. Chem. Res.* **2015**, *48* (1), 65–72.
24. Tan, C.; Cao, X.; Wu, X.-J.; He, Q.; Yang, J.; Zhang, X.; Chen, J.; Zhao, W.; Han, S.; Nam, G.-H.; Sindoro, M.; Zhang, H. *Chem. Rev.* **2017**, *117* (9), 6225–6331.
25. Duong, D. L.; Yun, S. J.; Lee, Y. H. *ACS Nano* **2017**, *11* (12), 11803–11830.
26. Dewandre, A.; Verstraete, M. J.; Grobert, N.; Zanolli, Z. *J. Phys. Mater.* **2019**, *2* (4), 044005.
27. Bergeron, H.; Lebedev, D.; Hersam, M. C. *Chem. Rev.* **2021**, *121* (4), 2713–2775.
28. Jensen, W. B. *J. Chem. Educ.* **2003**, *80* (8), 952–961.
29. Rogalski, A.. *Rep. Prog. Phys.* **2005**, *68*, 2267–2336.
30. Mughal, M. A.; Engelken, R.; Sharma, R. *Sol. Energy* **2015**, *120*, 131–146.
31. Cao, T.; Shi, X.-L.; Li, M.; Hu, B.; Chen, W.; Liu, W. D.; Lyu, W.; MacLeod, J.; Chen, Z.-G. *eScience* **2023**, *3* (3), 100122.
32. LaLonde, A. D.; Pei, Y.; Wang, H.; Snyder, G. J. *Mater. Today* **2011**, *14* (11), 526–532.
33. Xiao, Y.; Zhao, L.-D. *Npj Quant. Mater.* **2018**, *3*, 55.
34. Cai, Z.-H.; Narang, P.; Atwater, H. A.; Chen, S.; Duan, C. G.; Zhu, Z.-Q.; Chu, J.-H. *Chem. Mater.* **2015**, *27* (22), 7757–7764.
35. Goodman, C. H. L. *J. Phys. Chem. Solid.* **1958**, *6* (4), 305–314.
36. Pamplin, B. R. *Nature* **1960**, *188*, 136–137.
37. Wang, C.; Chen, S.; Yang, J.-H.; Lang, L.; Xiang, H.-J.; Gong, X.-G.; Walsh, A.; Wei, S.-H. *Chem. Mater.* **2014a**, *26* (11), 3411–3417.
38. Jiang, T.; Ozin, G. A. *J. Mater. Chem.* **1998**, *8*, 1099–1108.
39. Antunez, P. D.; Buckley, J. J.; Brutchey, R. L. *Nanoscale* **2011**, *3*, 2399–2411.
40. Zhao, L. D.; Lo, S. H.; Zhang, Y.; Sun, H.; Tan, G.; Uher, C.; Wolverton, C.; Dravid, V. P.; Kanatzidis, M. G. *Nature* **2014**, *508*, 373–377.
41. Jiang, B.; Neu, J.; Olds, D.; Kimber, S. A. J.; Page, K.; Siegrist, T. *Nat. Commun.* **2023**, *14*, 3211.
42. Lewis, D. J.; Kevin, P.; Bakr, O.; Muryn, C. A.; Malik, M. A.; O'Brien, P. *Inorg. Chem. Front.* **2014**, *1*, 577–598.
43. Bletskan, D. I. J. *Ovonic Res.* **2005**, *1* (5), 61–69.
44. Skelton, J. M.; Burton, L. A.; Oba, F.; Walsh, A. *APL Mater.* **2017**, *5*, 036101.
45. Burton, L. A.; Walsh, A. *J. Phys. Chem. C* **2012**, *116* (45), 24262–24267.
46. Pallikara, I.; Skelton, J. M. *Phys. Chem. Chem. Phys.* **2021**, *23*, 19219–19236.
47. Iizumi, M.; Hamaguchi, Y.; Komatsubara, K. F.; Kato, Y. *J. Phys. Soc. Japan* **1975**, *38*, 443.
48. Kobayashi, K. L. I.; Kato, Y.; Katayama, Y.; Komatsubara, K. F. *Phys. Rev. Lett.* **1976**, *37*, 772.

49. Burton, L. A.; Colombara, D.; Abellon, R. D.; Grozema, F. C.; Peter, L. M.; Savenije, T. J.; Dennler, G.; Walsh, A. *Chem. Mater.* **2013**, *25* (24), 4908–4916.
50. Shimada, T.; Ohuchi, F. S.; Parkinson, B. A. *J. Vac. Sci. Technol. A* **1992**, *10*, 539–542.
51. He, F.; Klein, E.; Bartling, S.; Saeidpour, S.; Corzilius, B.; Lesyuk, R.; Klinke, C. *J. Phys. Chem. C* **2022**, *126*, 20498–20504.
52. Shen, J.; Jung, Y.; Disa, A. S.; Walker, F. J.; Ahn, C. H.; Cha, J. J. *Nano Lett.* **2014**, *14* (7), 4183–4188.
53. Mitzi, D. B.; Gunawan, O.; Todorov, T. K.; Wang, K.; Guha, S. *Sol. Energy Mater. Sol. Cell.* **2011**, *95* (6), 1421–1436.
54. Banik, A.; Roychowdhury, S.; Biswas, K. *Chem. Commun.* **2018**, *54*, 6573–6590.
55. Fiechter, S.; Martinez, M.; Schmidt, G.; Henrion, W.; Tomm, Y. *J. Phys. Chem. Solid.* **2003**, *64* (9–10), 1859–1862.
56. Lokhande, A. C.; Babar, P. T.; Karade, V. C.; Gang, M. G.; Lokhande, V. C.; Lokhande, C. D.; Kim, J. H. *J. Mater. Chem. A* **2019**, *7*, 17118–17182.
57. Bourgès, C.; Lemoine, P.; Lebedev, O. I.; Daou, R.; Hardy, V.; Malaman, B.; Guilmeau, E.. *Acta Mater.* **2015**, *97*, 180–190.
58. Ahmadi, M.; Pramana, S. S.; Batabyal, S. K.; Boothroyd, C.; Mhaisalkar, S. G.; Lam, Y. M. *Inorg. Chem.* **2013**, *52* (4), 1722–1728.
59. Chen, S.; Walsh, A.; Luo, Y.; Yang, J. H.; Gong, X. G.; Wei, S. H. *Phys. Rev. B: Condens. Matter Mater. Phys.* **2010**, *82*, 195203.
60. Engberg, S.; Symonowicz, J.; Schou, J.; Canulescu, S.; Jensen, K. M. Ø. *ACS Omega* **2020**, *5* (18), 10501–10509.
61. Khare, A.; Himmetoglu, B.; Johnson, M.; Norris, D. J.; Cococcioni, M.; Aydil, E. S. *J. App. Phys.* **2012**, *111*, 083707–083715.
62. Pinto, A. H.; Shin, S. W.; Isaac, E.; Knutson, T. R.; Aydil, E. S.; Penn, R. L. *J. Mater. Chem. A* **2017**, *5*, 23179–23189.
63. Bosson, C. J.; Birch, M. T.; Halliday, D. P.; Knight, K. S.; Gibbs, A. S.; Hatton, P. D. *J. Mater. Chem. A* **2017**, *5*, 16672–16680.
64. Chang, J.; Waclawik, E. R. *RSC Adv.* **2014**, *4*, 23505–23527.
65. Jiang, H.; Dai, P.; Feng, Z.; Fan, W.; Zhan, J. *J. Mater. Chem.* **2012**, *22*, 7502–7506.
66. Syafiq, U.; Ataollahi, N.; Di Maggio, R.; Scardi, P. *Molecules* **2019**, *24* (19), 3454.
67. Wang, J.-J.; Liu, P.; Seaton, C. C.; Ryan, K. M. *J. Am. Chem. Soc.* **2014b**, *136* (22), 7954–7960.
68. Mainz, R.; Singh, A.; Levcenko, S.; Klaus, M.; Genzel, C.; Ryan, K. M.; Unold, T. *Nat. Commun.* **2014**, *5*, 3133.
69. Chen, S.; Gong, X. G.; Walsh, A.; Wei, S.-H. *Appl. Phys. Lett.* **2009**, *94*, 041903.
70. Dimitrievska, M.; Boero, F.; Litvinchuk, A. P.; Delsante, S.; Borzone, G.; Perez-Rodriguez, A.; Izquierdo-Roca, V. *Inorg. Chem.* **2017**, *56* (6), 3467–3474.
71. Ramkumar, S. P.; Gillet, Y.; Miglio, A.; van Setten, M. J.; Gonze, X.; Rignanese, G.-M. *Phys. Rev. B* **2016**, *94*, 224302.
72. Norris, D. J.; Bawendi, M. G. *Phys. Rev. B: Condens. Matter Mater. Phys.* **1996**, *53*, 16338–16346.
73. Steigerwald, M. L.; Brus, L. E. *Acc. Chem. Res.* **1990**, *23* (6), 183–188.
74. Brent, J. R.; Lewis, D. J.; Lorenz, T.; Lewis, E. A.; Savjani, N.; Haigh, S. J.; Seifert, G.; Derby, B.; O'Brien, P. *J. Am. Chem. Soc.* **2015**, *137* (39), 12689–12696.
75. Gonzalez, J. M.; Oleynik, I. I. *Phys. Rev. B* **2016**, *94*, 125443.
76. Shi, W.; Gao, M.; Wei, J.; Gao, J.; Fan, C.; Ashalley, E.; Li, H.; Wang, Z. *Adv. Sci.* **2018**, *5* (4), 1700602.
77. Tritsaris, G. A.; Malone, B. D.; Kaxiras, E. *J. Appl. Phys.* **2013**, *113*, 233507.
78. Shinde, P.; Rout, C. S. *Mater. Chem. Front.* **2021**, *5*, 516–556.
79. Bletskan, D. I. *Chalcogenide Lett.* **2007**, *4* (1), 1–16.
80. Shah, K. W.; Wang, S.-X.; Zheng, Y.; Xu, J. *Appl. Sci.* **2019**, *9* (7), 1511.
81. Aldakov, D.; Lefrancois, A.; Reiss, P. *J. Mater. Chem. C* **2013**, *1*, 3756–3776.
82. Khan, M. D.; Opallo, M.; Revaprasadu, N. *Dalton Trans.* **2021**, *50*, 11347–11359.
83. Kumar, M.; Rani, S.; Singh, Y.; Gour, K. S.; Singh, V. N. *RSC Adv.* **2021**, *11*, 6477–6503.
84. Reiss, P.; Carriere, M.; Lincheneau, C.; Vaure, L.; Tamang, S. *Chem. Rev.* **2016**, *116* (18), 10731–10819.
85. Yin, D.; Dun, C.; Gao, X.; Liu, Y.; Zhang, X.; Carroll, D. L.; Swihart, M. T. *Small* **2018**, *14* (33), 1801949.
86. Ahmet, I. Y.; Thompson, J. R.; Johnson, A. L. *Eur. J. Inorg. Chem.* **2018a**, *2018* (15), 1670–1678.
87. Brune, V.; Raydan, N.; Sutorius, A.; Hartl, F.; Purohit, B.; Gahlot, S.; Bargiela, P.; Burel, L.; Wilhelm, M.; Hegemann, C.; Atamtürk, U.; Mathur, S.; Mishra, S. *Dalton Trans.* **2021**, *50*, 17346–17360.
88. Feng, D.; Ge, Z.-H.; Chen, Y.-X.; Li, J.; He, J. *Nanotechnology* **2017**, *28*, 455707.
89. Tripathi, A. M.; Mitra, S. *RSC Adv.* **2014**, *4*, 10358–10366.
90. Kedarnath, G.; Jain, V. K. *New J. Chem.* **2023**, *47*, 20688.
91. Jain, V. K.; Kedarnath, G. Applications of Metal-Selenium and/-tellurium Compounds in Materials Science. In *Selenium and tellurium reagents in chemistry and materials science*; Laitinen, R.; Oilunkaniemi, R., Eds.; Walther de Gruyter: Germany, 2019; pp. 383–443.
92. Jain, V. K.; Chauhan, R. S. Metal Chalcogenolates: Synthesis and Applications to Materials Science. In *Chalcogen Chemistry: Fundamentals and Applications*; Lippolis, V.; Santi, C.; Lenardao, E. J.; Braga, A. L., Eds.; Royal Society of Chemistry: UK, 2023; pp. 58–82.
93. Karmakar, G.; Tyagi, A.; Shah, A. Y. *Coord. Chem. Rev.* **2024**, *504*, 215665.
94. Boudjouk, P.; Seidler, D. J.; Grier, D.; McCarthy, G. *J. Chem. Mater.* **1996**, *8* (6), 1189–1196.
95. Orava, J.; Kohoutek, T.; Wagner, T. Deposition Techniques for Chalcogenide Thin Films. In *Chalcogenide Glasses: Preparation, Properties and Applications*; Adam, J.-L., Zhang, X., Eds.; Woodhead: Cambridge, UK, 2014; pp 265–309.
96. Hitchcock, P. B.; Lappert, M. F.; Samways, B. J.; Weinberg, E. L. *J. Chem. Soc., Chem. Commun.* **1983**, 1492–1494. https://doi.org/10.1039/C39830001492.
97. Cheng, Y.; Emge, T. J.; Brennan, J. G. *Inorg. Chem.* **1996**, *35* (2), 342–346.
98. Seligson, A. L.; Arnolds, J. *J. Am. Chem. Soc.* **1993**, *115*, 8214–8220.
99. Zemlyanskii, N. N.; Borisova, I. V.; Kuznetsova, M. G.; Khrustalev, E. N.; Antipin, M.Yu.; Ustynyuk, Yu. A.; Lunin, E. E.; Eaborn, C.; Hill, M. S.; Smith, J. D. *Russ. J. Org. Chem.* **2003**, *39*, 491–500.
100. Veith, M.; Hobein, P.; Rösler, R. *Z. Naturforsch. B* **1989**, *44* (9), 1067–1081.
101. Eichhofer, A.; Jiang, J. J.; Sommer, H.; Weigand, F.; Fuhr, O.; Fenske, D.; Su, C. Y.; Buth, G. *Eur. J. Inorg. Chem.* **2010**, *2010* (3), 410–418.
102. Kovalenko, M. V.; Heiss, W.; Shevchenko, E. V.; Lee, J.-S.; Schwinghammer, H.; Alivisatos, A. P.; Talapin, D. V. *J. Am. Chem. Soc.* **2007**, *129* (37), 11354–11355.
103. Park, J.; Song, M.; Jung, W. M.; Lee, W. Y.; Lee, J.; Kim, H.; Shim, I.-W. *Bull. Kor. Chem. Soc.* **2012**, *33* (10), 3383–3386.
104. Park, J. H.; Kang, S. G.; Lee, Y. K.; Chung, T. M.; Park, B. K.; Kim, C. G. *Inorg. Chem.* **2020**, *59* (6), 3513–3517.
105. Catherall, A. L.; Harris, S.; Hill, M. S.; Johnson, A. L.; Mahon, M. F. *Cryst. Growth Des.* **2017**, *17* (10), 5544–5551.
106. Ahmet, I. Y.; Hill, M. S.; Johnson, A. J.; Peter, L. M. *Chem. Mater.* **2015**, *27* (22), 7680–7688.

107. Atamtürk, U.; Brune, V.; Mishra, S.; Mathur, S. *Molecules* **2021**, *26* (17), 5367.
108. Kevin, P.; Malik, S. J.; Malik, M. A.; O'Brien, P. *Chem. Commun.* **2014**, *50*, 14328–14330.
109. Kevin, P.; Lewis, D. J.; Raftery, J.; Malik, M. A.; O'Brien, P. *J. Cryst. Growth* **2015**, *415*, 93–99.
110. Koktysh, D. S.; McBride, J. R.; Rosenthal, S. R. *Nanoscale Res. Lett.* **2017**, *2*, 144–148.
111. Zhang, Y.; Lu, J.; Chen, S.; Xu, H.; Wang, Q. *Chem. Commun.* **2011**, *47*, 5226–5228.
112. Hibbert, T. G.; Mahon, M. F.; Molloy, K. C.; Price, L. S.; Parkin, I. P. *J. Mater. Chem.* **2011**, *21*, 469–473.
113. Barone, G.; Hibbert, T. G.; Mahon, M. F.; Molloy, K. C.; Price, L. S.; Parkin, I. P.; Hardy, A. M. F.; Field, M. N. *J. Mater. Chem.* **2001**, *11*, 464–468.
114. Parkin, I. P.; Price, L. S.; Hibbert, T. G.; Molloy, K. C. *J. Mater. Chem.* **2001**, *11*, 1486–1490.
115. Schlecht, S.; Budde, M.; Kienle, L. *Inorg. Chem.* **2002**, *41* (23), 6001–6005.
116. Hartl, F.; Brune, V.; Lüggert, S.; Hegemann, C.; van Gerven, D.; Wilhelm, M.; Ji, S.; Choi, H.; Mathur, S. *Inorg. Chem.* **2023**, *62* (16), 6274–6287.
117. Thompson, J. R.; Ahmet, I. Y.; Johnson, A. L.; Kociok-Köhn, G. *Eur. J. Inorg. Chem.* **2016**, *2016* (28), 4711–4720.
118. Robinson, F.; Curran, P. J.; de Groot, C. H.; Hardie, D.; Hector, A. L.; Holloway, K.; Huang, R.; Newbrook, D.; Reid, G. *Mater. Adv.* **2021a**, *2*, 4814–4823.
119. Robinson, F.; Newbrook, D. W.; Curran, P.; de Groot, C. H.; Hardie, D.; Hector, H. L.; Huang, R.; Reid, G. *Dalton Trans.* **2021b**, *50*, 998–1006.
120. Jain, V. K. *Dalton Trans.* **2020**, *49*, 8817–8835.
121. Karmakar, G.; Halankar, K. K.; Tyagi, A.; Mandal, B. P.; Wadawale, A.; Kedarnath, G.; Srivastava, A. P.; Singh, V. *Dalton Trans.* **2021**, *50*, 15730–15742.
122. Karmakar, G.; Tyagi, A.; Shah, A. Y.; Wadawale, A.; Kedarnath, G.; Singh, V. *Polyhedron* **2022**, *220*, 115833.
123. Sharma, R. K.; Kedarnath, G.; Wadawale, A.; Betty, C. A.; Vishwanadh, B.; Jain, V. K. *Dalton Trans.* **2012**, *41*, 12129–12138.
124. Tyagi, A.; Kedarnath, G.; Wadawale, A.; Jain, V. K.; Kumar, M.; Vishwanadh, B. *RSC Adv.* **2015**, *5*, 62882–62890.
125. Tyagi, A.; Kedarnath, G.; Wadawale, A.; Shah, A. Y.; Jain, V. K.; Vishwanadh, B. *RSC Adv.* **2016**, *6*, 8367–8376.
126. Tyagi, A.; Karmakar, G.; Wadawale, A.; Shah, A. Y.; Kedarnath, G.; Srivastava, A. P.; Singh, V.; Jain, V. K. *J. Organomet. Chem.* **2018a**, *873*, 15–21.
127. Tyagi, A.; Shah, A. Y.; Kedarnath, G.; Wadawale, A.; Singh, V.; Tyagi, D.; Betty, C. A.; Lal, C.; Jain, V. K. *J. Mater. Sci. Mater. Elect.* **2018b**, *29*, 8937–8946.
128. Tyagi, A.; Kole, G. K.; Shah, A. Y.; Wadawale, A.; Srivastava, A. P.; Kumar, M.; Kedarnath, G.; Jain, V. K. *J. Organomet. Chem.* **2019**, *887*, 24–31.
129. Tyagi, A.; Karmaker, G.; Mandal, B. P.; Pathak, D. D.; Wadawale, A.; Kedarnath, G.; Srivastava, A. P.; Jain, V. K. *Dalton Trans.* **2021**, *50*, 13073–13085.
130. Al-Shakban, M.; Metthews, P. D.; Lewis, E. A.; Raftery, J.; Vitorica-Yrezabal, I.; Haigh, H. J.; Lewis, D. L.; O'Brien, P. *J. Mater. Sci.* **2019**, *54*, 2315–2323.
131. Barone, G.; Chaplin, T.; Hibbert, T. G.; Kana, A. T.; Mahon, M. F.; Molly, K. C.; Worsley, I. D.; Perkin, I. P.; Price, L. S. *J. Chem. Soc. Dalton Trans.* **2002**, 1085–1092. https://doi.org/10.1039/B108509N.
132. Kana, A. T.; Hibbert, T. G.; Mahon, M. F.; Molloy, K. C.; Perkin, I. P.; Price, L. S. *Polyhedron* **2001**, *20*, 2989–2995.
133. Khan, M. D.; Akhtar, J.; Malik, M. A.; Akhtar, M.; Revaprasadu, N. *New J. Chem.* **2015**, *39*, 9569–9574.
134. Ramasamy, K.; Kuznetsov, V. I.; Gopal, K.; Malik, M. A.; Raftery, J.; Edwards, P. P.; O'Brien, P. *Chem. Mater.* **2013**, *25* (3), 266–276.
135. Khan, M. D.; Aamir, M.; Sohail, M.; Sher, M.; Baig, N.; Akhtar, J.; Malik, M. A.; Revaprasadu, N. *Dalton Trans.* **2018a**, *47*, 5465–5473.
136. Khan, M. D.; Aamir, M.; Murtaza, G.; Malik, M. A.; Revaprasadu, N. *Dalton Trans.* **2018b**, *47*, 10025–10034.
137. Bahr, S. R.; Boudjouk, P.; McCarthy, G. *J. Chem. Mater.* **1992**, *4*, 383–388.
138. Boudjouk, P.; Seidler, D. J.; Bahr, S. R.; McCarthy, G. *J. Chem. Mater.* **1994**, *6*, 2108–2112.
139. Boudjouk, P.; Remington, M. P. Jr.; Grier, D. G.; Triebold, W.; Jarabek, B. R. *Organometallics* **1999**, *18* (22), 4534–4537.
140. Chuprakov, I. S.; Dahmen, K.-H.; Schneider, J. J. Hagen, J. *Chem. Mater.* **1998**, *10* (11), 3467–3470.
141. Schneider, J. J.; Hagen, J.; Heinemann, O.; Bruckmann, J.; Kruger, C. *Thin Solid Films* **1997**, *304* (1–2), 144.
142. Ahmet, I. Y.; Hill, M. S.; Raithby, P. R.; Johnson, A. L. *Dalton Trans.* **2018b**, *47*, 5031–5048.
143. de Groot, C. H.; Gurnani, C.; Hector, A. L.; Huang, R.; Jura, M.; Levason, W.; Reid, G. *Chem. Mater.* **2012**, *24* (22), 4442–4449.
144. Gurnani, G.; Hawken, S. L.; Hector, A. L.; Huang, R.; Jura, M.; Levason, W.; Perkins, J.; Reid, G.; Stenning, G. B. G.. *Dalton Trans.* **2018**, *47*, 2628–2637.
145. Reid, S. D.; Hector, A. L.; Levason, W.; Reid, G.; Waller, B. J.; Webster, M. . *Dalton Trans.* **2007**, 4769–4777. https://doi.org/10.1039/B708809D.
146. Boscher, N. D.; Carmalt, C. J.; Palgrave, R. G.; Parkin, I. P. *Thin Solid Films* **2008**, *516* (15), 4750–4757.
147. Price, L. S.; Parkin, I. P.; Hardy, A. M. E.; Clark, R. J. H.; Hibbert, T. G.; Molloy, K. C. *Chem. Mater.* **1999**, *11* (7), 1792–1799.
148. Manasevit, H. M.; Simpson, W. I. *J. Electrochem. Soc.* **1975**, *122* (3), 444.
149. Bade, B. P.; Garje, S. S.; Niwate, Y. S.; Afzal, M.; O'Brien, P. *Chem. Vap. Deposit.* **2008**, *14* (9–10), 292–295.
150. Banik, A.; Biswas, K. *J. Mater. Chem. A* **2014**, *2*, 9620–9625.
151. Mitzi, D. B.; Kosbar, L. l.; Murray, C. E.; Cope, M.; Afzall, A. *Nature* **2004**, *428*, 299–303.
152. Bouška, M.; Dostál, L.; de Proft, F.; Růžička, A.; Lyčka, A.; Jambor, R. *Chem. Eur J.* **2011**, *17* (2), 455–459.
153. Bouska, M.; Strizik, L.; Dostal, L.; Ruzicka, A.; Lyčka, A.; Benes, L.; Vlcek, M.; Prikryl, J.; Knotek, P.; Wagner, T.; Jambor, R. *Chem. Eur J.* **2013**, *19* (6), 1877–1881.
154. Wei, H.; Su, Y.; Chen, S.; Lin, Y.; Yang, Z.; Chen, X.; Zhang, Y. *J. Mater. Chem.* **2011a**, *21*, 12605–12608.
155. Im, H. S.; Myung, Y.; Cho, Y. J.; Kim, C. H.; Kim, H. S.; Back, S. H.; Jung, C. S.; Jang, D. M.; Lim, Y. R.; Park, J.; Ahn, J.-P. *RSC Adv.* **2013**, *3*, 10349–10354.
156. Abraham, T.; Juhasz, C.; Silver, J.; Donaldson, J. D.; Thomas, M. J. K. *Solid State Commun.* **1978**, *27* (11), 1185–1187.
157. Buckley, J. J.; Rabuffetti, F. A.; Hinton, H. L.; Brutchey, R. L. *Chem. Mater.* **2012**, *24* (18), 3514–3516.
158. Shah, A. Y.; Tyagi, A.; Kedarnath, G.; Betty, C. A.; Jain, V. K.; Vishwanath, B. Thermans-**2022**. In *Proceedings of DAE-BRNS Symposium on Thermal Analysis- Thermal Techniques for Advanced Materials*; THERMANS: Mumbai, India, 2022.
159. Wei, H.; Su, Y.; Chen, S.; Lin, Y.; Yang, Z.; Sunc, H.; Zhang, Y. *CrystEngComm* **2011b**, *13*, 6628–6631.
160. Arachchige, I. U.; Kanatzidis, M. G. *Nano Lett.* **2009**, *9* (4), 1583–1587.

161. Li, B.; Xie, Y.; Huang, J.; Qian, Y. *J. Sol. State Chem.* **2000**, *153* (1), 170.
162. Liang, X.; Cai, Q.; Xiang, W.; Chen, Z.; Zhong, J.; Wang, Y.; Shao, M.; Li, Z. *J. Mater. Sci. Technol.* **2013**, *29* (3), 231.
163. Tan, Y.; Lin, Z.; Ren, W.; Long, W.; Wang, Y.; Ouyang, X. *Mater. Lett.* **2012**, *89*, 240.
164. Ge, Z.-H.; Salvador, J. R.; Nolas, G. S. *Inorg. Chem.* **2014**, *53* (9), 4445–4449.
165. Ibañez, M.; Cadavid, D.; Anselmi-Tamburini, U.; Zamani, R.; Gorsse, S.; Li, W.; Lopez, A. M.; Morante, J. R.; Arbiol, J.; Cabot, A. *J. Mater. Chem. A* **2013**, *1*, 1421–1426.
166. Jeong, J.; Chung, H.; Ju, Y. C.; Moon, J.; Roh, J.; Yoon, S.; Do, Y. R.; Kim, W. *Mater. Lett.* **2010**, *64* (19), 2043.
167. Li, S.; Pan, D. *J. Cryst. Growth* **2012**, *358*, 38–42.
168. Liang, Q.; Han, L.; Deng, X.; Yao, C.; Meng, J.; Liu, X.; Meng, J. *CrystEngComm* **2014**, *16*, 4001–4007.
169. Norako, M. E.; Greaney, M. J.; Brutchey, R. L. *J. Am. Chem. Soc.* **2012**, *134* (1), 23–26.
170. Wang, J.; Singh, A.; Liu, P.; Singh, S.; Coughlan, C.; Guo, Y.; Ryan, K. M. *J. Am. Chem. Soc.* **2013**, *135* (21), 7835–7838.
171. Coughlan, C.; Ibañez, M.; Dobrozhan, O.; Singh, A.; Cabot, A.; Ryan, K. M. *Chem. Rev.* **2017**, *117* (9), 5865–6109.
172. Liu, Q.; Zhao, Z.; Lin, Y.; Guo, P.; Li, S.; Pan, D.; Ji, X. *Chem. Commun.* **2011**, *47*, 964–966.
173. Chang, J.; Waclawik, E. R. *CrystEngComm* **2013**, *15*, 5612–5619.
174. Wang, J. J.; Ryan, K. M. *CrystEngComm* **2016**, *18*, 3161–3169.
175. Fan, J.; Carrillo-Cabrera, W.; Akselrud, L.; Antonyshyn, I.; Chen, L.; Grim, Y. *Inorg. Chem.* **2013**, *52* (19), 11067–11074.
176. Macrae, C. F.; Edgington, P. R.; McCabe, P.; Pidcock, E.; Shields, G. P.; Taylor, R.; Towler, M.; van der Streek, J. *J. Appl. Crystallogr.* **2006**, *39*, 453–457.
177. Yi, L.; Wang, D.; Gao, M. *CrystEngComm* **2012**, *14*, 401–404.
178. Jishi, R. A.; Lucas, M. A.; Internat., J. *Photoenergy* **2016**, ID6193502; https://doi.org/10.1155/2016/6193502.
179. Jia, H.; Dirican, M.; Sun, N.; Chen, C.; Yan, C.; Zhu, P.; Dong, X.; Du, Z.; Cheng, H.; Guo, J.; Zhang, X. *Chemelectrochem* **2019**, *6* (4), 1183–1191.
180. Mohsin, M.; Bhunia, S.; Nayak, A. *J. Mater. Sci. Mater. Electron.* **2023**, *34*, 2194.
181. Sun, D.; Xiong, Y.; Sun, Y.; Dabo, I.; Schaak, R. E. *Chem. Mater.* **2017**, *29* (3), 1095–1098.
182. Fan, F.-J.; Wu, L.; Yu, S.-H. *Energy Environ. Sci.* **2014**, *7*, 190–208.
183. Camara, S. M.; Wang, L.; Zhang, X. *Nanotechnology* **2013**, *24* (49), 495401.
184. Henríquez, R.; Nogales, P. S.; Moreno, P. G.; Cartagena, E. M.; Bongiorno, P. L.; Navarrete-Astorga, E.; Dalchiele, E. A. *Nanomaterials* **2023**, *13* (11), 1731.
185. Mirbagheri, N.; Engberg, S.; Crovetto, A.; Simonsen, S. B.; Hansen, O.; Lam, Y. M.; Schou, J. *Nanotechnology* **2016**, *27* (18), 185603.
186. Singh, A.; Geaney, H.; Laffir, F.; Ryan, K. M. *J. Am. Chem. Soc.* **2012**, *134* (6), 2910–2913.
187. Long, F.; Chi, S.; He, J.; Wang, J.; Wu, X.; Mo, S.; Zou, Z. *J. Sol. State Chem.* **2015**, *229*, 228–234.
188. Murtaza, G.; Alderhami, S.; Alharbi, Y. T.; Zulfiqar, U.; Hossin, M.; Alanazi, A. M.; Almanqur, L.; Onche, E. U.; Venkateswaran, S. P.; Lewis, D. J. *ACS Appl. Energy Mater.* **2020**, *3* (2), 1952–1961.
189. Ramasamy, K.; Malik, M. A.; O'Brien, P. *Chem. Sci.* **2011**, *2*, 1170–1172.
190. Regulacio, M. D.; Ye, C.; Lim, S. H.; Bosman, M.; Ye, E.; Chen, S.; Xu, Q.-H.; Han, M.-Y. *Chem. Eur J.* **2012**, *18* (11), 3127–3131.
191. Zou, C.; Zhang, L.; Lin, D.; Yang, Y.; Li, Q.; Xu, X.; Chen, X.; Huang, S. *CrystEngComm* **2011**, *13*, 3310–3313.
192. Al-Shakban, M.; Matthews, P. D.; Savjani, N.; Zhong, X. L.; Wang, Y.; Missous, M.; O'Brien, P. *J. Mater. Sci.* **2017**, *52*, 12761–12771.
193. Lu, X.; Zhuang, Z.; Peng, Q.; Li, Y. *Chem. Commun.* **2011**, *47*, 3141–3143.
194. Shavel, A.; Arbiol, J.; Cabot, A. *J. Am. Chem. Soc.* **2010**, *132* (13), 4514–4515.
195. Jin, C.; Ramasamy, P.; Kim, J. *Dalton Trans.* **2014**, *43*, 9481–9485.
196. Fuhrmann, D.; Dietrich, S.; Krautscheid, H. *Inorg. Chem.* **2017**, *56* (21), 13123–13131.
197. Rath, T.; Haas, W.; Pein, A.; Saf, R.; Maier, E.; Kunert, B.; Hofer, F.; Resel, R.; Trimmel, G. *Sol. Energy Mater. Sol. Cell.* **2012**, *101*, 87.
198. Zou, Y.; Su, X.; Jiang, J. *J. Am. Chem. Soc.* **2013**, *135* (49), 18377–18384.
199. Zhang, X.; Guo, G.; Ji, C.; Huang, K.; Zha, C.; Wang, Y.; Shen, L.; Gupta, A.; Bao, N. *Sci. Rep.* **2014b**, *4*, 5086.
200. Isacfranklin, M.; Yuvakkumar, R.; Ravi, G.; Saravanakumar, B.; Pannipara, M.; Al-Sehemi, A. G.; Velauthapillai, D. *ACS Omega* **2021a**, *6* (14), 9471–9481.
201. Manjula, S.; Sivakumar, G.; Dhamodharan, P.; Dinesh, A.; Jaganathan, S. K.; Ayyar, M. Z. *Phys. Chem.* **2024**, *238* (3), 437–457.
202. Sarkar, S.; Howli, P.; Ghorai, U. K.; Das, B.; Samanta, M.; Das, N. S.; Chattopadhyay, K. K. *CrystEngComm* **2018**, *20*, 1443–1454.
203. Vanalakara, S. A.; Patil, P. S.; Kim, J. H. *Sol. Energy Mater. Sol. Cell.* **2018**, *182*, 204–219.
204. Rondiya, S.; Wadnerkar, N.; Jadhav, Y.; Jadkar, S.; Haram, S.; Kabir, M. *Chem. Mater.* **2017**, *29* (7), 3133–3142.
205. Nie, L.; Yang, J.; Yang, D.; Liu, S. *J. Mater. Sci. Mater. Electron.* **2019**, *30*, 3760–3766.
206. Chen, L.; Deng, H.; Tao, J.; Cao, H.; Huang, L.; Sun, L.; Yang, P.; Chu, J. *RSC Adv.* **2015a**, *5*, 84295–84302.
207. Chen, L. L.; Deng, H. M.; Zhang, K. Z.; Huang, L.; Liu, J.; Sun, L.; Yang, P. X.; Chu, J. H. *Mater. Sci. Forum* **2015b**, *814*, 39–43.
208. Krishnaiah, M.; Bhargava, P.; Mallick, S. *RSC Adv.* **2015**, *5*, 96928–96933.
209. Murali, B.; Madhuri, M.; Krupanidhi, S. B. *Cryst. Growth Des.* **2014**, *14* (8), 3685–3691.
210. Beraich, M.; Taibi, M.; Guenbour, A.; Zarrouk, A.; Boudalia, M.; Bellaouchou, A.; Tabyaoui, M.; Sekkat, Z.; Fahoume, M. *J. Mater. Sci. Mater. Electron.* **2019**, *30*, 12487–12492.
211. Cui, Y.; Deng, R.; Wang, G.; Pan, D. A. *J. Mater. Chem.* **2012**, *22*, 23136–23140.
212. Yan, C.; Huang, C.; Yang, J.; Liu, F.; Liu, J.; Lai, Y.; Li, J.; Liu, Y. *Chem. Commun.* **2012**, *48*, 2603–2605.
213. Zhang, X.; Bao, N.; Ramasamy, K.; Wang, Y.-H. A.; Wang, Y.; Lin, B.; Gupta, A. *Chem. Commun.* **2012**, *48*, 4956–4958.
214. Chane-Ching, J. Y.; Gillorin, A.; Zaberca, O.; Balocchi, A.; Marie, X. *Chem. Commun.* **2011**, *47*, 5229–5231.
215. Gillorin, A.; Balocchi, A.; Marie, X.; Dufour, P.; Chane-Ching, J. Y. *J. Mater. Chem.* **2011**, *21*, 5615–5619.
216. Zhang, X.; Bao, N.; Lin, B.; Gupta, A. *Nanotechnology* **2013b**, *24* (10), 105706.
217. Waluś, E.; Manecki, M.; Cios, G.; Tokarski, T. *Materials* **2021**, *14* (13), 3457.
218. Liang, X.; Guo, P.; Wang, G.; Deng, R.; Pan, D.; Wei, X. *RSC Adv.* **2012**, *2*, 5044–5046.
219. Norton, K. J.; Alam, F.; Lewis, D. *J. Appl. Sci.* **2021**, *11*, 2062.
220. Wilson, J. A.; Yoffe, A. D. *Adv. Phys.* **1969**, *18* (73), 193–335.
221. Han, S.; Shih, W. Y.; Shih, W.-H. *Chem. Sel.* **2017**, *2* (24), 7332–7339.
222. Chowdhury, A. P.; Shambharkar, B. H.; Ghugal, S. G.; Umare, S. S.; Shende, A. G. *RSC Adv.* **2016**, *6*, 108290–108297.

223. Bhorde, A.; Pawbake, A.; Sharma, P.; Nair, S.; Funde, A.; Bankar, P.; More, M.; Jadkar, S. *Appl. Phys. Mater. Sci. Process* **2018**, *124*, 133.
224. Franzman, M. A.; Schlenker, C. W.; Thompson, M. E.; Brutchey, R. L. *J. Am. Chem. Soc.* **2010**, *132* (12), 4060–4061.
225. Pastsuzak, J.; Wegierek, P. *Materials* **2022**, *15* (16), 5542.
226. Hayat, M. B.; Ali, D.; Monyake, K. C.; Alagha, L.; Ahmed, N. *Int. J. Energy Res.* **2019**, *43*, 1049–1067.
227. Rühle, S. *Sol. Energy* **2016**, *130*, 139–147.
228. Ahmet, I. Y.; Guc, M.; Sanchez, Y.; Neuschitzer, M.; Izquerdo-Roca, V.; Saucedo, E.; Johnson, A. L. *RSC Adv.* **2019**, *9*, 14899–14909.
229. Sinsermsuksakul, P.; Sun, L.; Lee, S. W.; Park, H. H.; Kim, S. B.; Yang, C.; Gordon, R. G. *Adv. Energy Mater.* **2014**, *4* (15), 1400496.
230. Hu, Z.; O'Neill, R.; Lesyuk, R.; Klinke, C. *Acc. Chem. Res.* **2021**, *54* (20), 3792–3803.
231. Jamali-Sheini, F.; Cheraghizade, M.; Yousefi, R. *Sol. Energy Mater. Sol. Cell.* **2016**, *154*, 49–56.
232. Mukai, K.; Wanibuchi, R.; Nunomura, Y. *J. Mater. Sci. Mater. Electron.* **2024**, *35*, 680.
233. Lokhande, A. C.; Chalapathy, R. B. V.; He, M.; Jo, E.; Gang, M.; Pawar, S. A.; Lokhande, C. D.; Kim, J. H. *Sol. Energy Mater. Sol. Cell.* **2016**, *153*, 84–107.
234. Reddy, V. R. M.; Pallavolu, M. R.; Guddeti, P. R.; Gedi, S.; Reddy, K. K. Y. B.; Pejjai, B.; Kim, W. K.; Kotte, T. R. R.; Park, C. *J. Ind. Eng. Chem.* **2019**, *76*, 39–74.
235. Tiwari, D.; Chaudhuri, T. K.; Shripathi, D.; Deshpande, U.; Rawat, R. *Sol. Energy Mater. Sol. Cell.* **2013**, *113*, 165–170.
236. Heidariramsheh, M.; Mirhosseini, M.; Abdizadeh, K.; Mahdavi, S. M.; Taghavinia, N. *ACS Appl. Energy Mater.* **2021**, *4*, 5560–5573.
237. Singh, A.; Singh, S.; Levcenko, S.; Unold, T.; Laffir, F.; Rayan, K. M. *Angew. Chem. Int. Ed.* **2013**, *52* (35), 9120–9124.
238. Cui, X.; Sun, K.; Huang, J.; Yun, J. S.; Lee, C.-Y.; Yan, C.; Sun, H.; Zhang, Y.; Xue, C.; Eder, K.; Yang, L.; Cairney, J. M.; Seidel, J.; Ekins-Daukes, N. J.; Green, M.; Hoex, B.; Hao, X. *Energy Environ. Sci.* **2019**, *12*, 2751–2764.
239. Guo, Q.; Ford, G. M.; Yang, W.-C.; Walker, B. C.; Stach, E. A.; Hillhouse, H. W.; Agrawal, R. *J. Am. Chem. Soc.* **2010**, *132* (49), 17384–17386.
240. Wang, H.; Intern, J. *Photoenergy* **2011**, *2011*, 801292.
241. Yan, C.; Huang, J.; Sun, K.; Johnston, S.; Zhang, Y.; Sun, H.; Pu, A.; He, M.; Liu, F.; Eder, K.; Yang, L.; Cairney, J. M.; Ekins-Daukes, N. J.; Hameiri, Z.; Stride, J. A.; Chen, S.; Green, M. A.; Hao, X. *Nat. Energy* **2018**, *3*, 764–772.
242. Todorov, T. K.; Tang, J.; Bag, S.; Gunawan, O.; Gokmen, T.; Zhu, Y.; Mitzi, D. B. *Adv. Energy Mater.* **2013**, *3*, 34–38.
243. Prabhakar, R. R.; Zhenghua, S.; Xin, Z.; Baikie, T.; Woei, L. S.; Shukla, S.; Batabyal, S. K.; Gunawan, O.; Wong, L. H. *Sol. Energy Mater. Sol. Cells* **2016**, *157*, 867–873.
244. Sheela, S. E.; Sekar, R.; Maurya, D. K.; Paulraj, M.; Angaiah, S. *Mater. Sci. Semicond. Proc.* **2023**, *156*, 107273.
245. Kumara, D. K.; Popuri, S. R.; Swami, S. K.; Onuoha, O. R.; Bos, J.-W. G.; Chen, B.; Bennett, N.; Upadhyaya, H. M. *Sol. Energy* **2019**, *190*, 28–33.
246. Ramasamy, P.; Manivasakan, P.; Kim, J. *CrystEngComm* **2015**, *17*, 807.
247. Yang, B.; Zuo, X.; Chen, P.; Zhou, L.; Yang, X.; Zhang, H.; Li, G.; Wu, M.; Ma, Y.; Jin, S.; Chen, X. S. *ACS Appl. Mater. Interfaces* **2015**, *7* (1), 137–143.
248. Yu, X.; Zhu, J.; Zhang, Y.; Weng, J.; Hu, L.; Dai, S. *Chem. Commun.* **2012**, *48*, 3324–3326.
249. Kedarnath, G.; Jain, V. K. Quantum Dots for Type III Photovoltaics. In *Nanostructured materials for type-III photovoltaics*; Skabara, P.; Malik, M. A., Eds.; Royal Society of Chemistry: UK, 2018; pp. 436–471.
250. Xin, X.; He, M.; Han, W.; Jung, J.; Lin, Z. *Angew. Chem. Int. Ed.* **2011**, *50* (49), 11739–11742.
251. Zhang, X.; Xu, Y.; Zhang, J.; Dong, S.; Shen, L.; Gupta, A.; Bao, N. *Sci. Rep.* **2018**, *8*, 248.
252. Chia, X.; Lazar, P.; Sofer, Z.; Luxa, J.; Pumera, M. *J. Phys. Chem. C* **2016**, *120* (42), 24098–24111.
253. Sun, Y.; Cheng, H.; Gao, S.; Sun, Z.; Liu, Q.; Liu, Q.; Lei, F.; Yao, T.; He, J.; Wei, S.; Xie, Y. *Angew. Chem. Int. Ed. Engl.* **2012**, *124* (35), 8857–8861.
254. Li, G.; Su, R.; Rao, J.; Wu, J.; Rudolf, P.; Blake, G. R.; de Groot, R. A.; Besenbacher, F.; Palstra, T. T. M. *J. Mater. Chem. A* **2016**, *4*, 209–216.
255. Vadivel, S.; Maruthamani, D.; Paul, B.; Dhar, S. S.; Habibi-Yangjeh, A.; Balachandran, S.; Saravanakumar, B.; Selvakumar, A.; Selvam, K. *RSC Adv.* **2016**, *6*, 74177–74185.
256. Zaman, M. B.; Chandel, T.; Poolla, R. *Mater. Res. Exp.* **2019**, *6* (2), 025004.
257. Das, H. T.; Dutta, S.; Gaurav, K.; Giri, A. K.; Mondal, A.; Jena, R. K.; Das, N. *Chem. Asian J.* **2023**, *19* (16), e202300813.
258. Yang, Y.; Ding, Y.; Zhang, J.; Liang, N.; Long, L.; Liu, J. *Nanomaterials* **2022**, *12* (9), 1439.
259. Poudel, B.; Hao, Q.; Ma, Y.; Lan, Y.; Minnich, A.; Yu, B.; Yan, X.; Wang, D.; Muto, A.; Vashaee, D.; Chen, X.; Liu, J.; Dresselhaus, M. S.; Chen, G.; Ren, Z. *Science* **2008**, *320* (5876), 634–638.
260. Hochbaum, A. I.; Yang, P. *Chem. Rev.* **2010**, *110* (1), 527–546.
261. Tian, Z.; Guo, C.; Zhao, M.; Li, R.; Xue, J. *ACS Nano* **2017**, *11* (2), 2219–2226.
262. Xin, C.; Zheng, J.; Su, Y.; Li, S.; Zhang, B.; Feng, Y.; Pan, F. *J. Phys. Chem. C* **2016**, *120* (39), 22663–22669.
263. Sandonas, L. M.; Teich, D.; Gutierrez, R.; Lorenz, T.; Pecchia, A.; Seifert, G.; Cuniberti, G. *J. Phys. Chem. C* **2016**, *120*, 18841–18849.
264. Zhang, H.; Talapin, D. V. *Angew. Chem. Int. Ed.* **2014a**, *53* (35), 9126–9127.
265. Zhao, L.-D.; Tan, G.; Hao, S.; He, J.; Pei, Y.; Chi, H.; Wang, H.; Gong, S.; Xu, H.; Dravid, V. P.; Uher, C.; Snyder, G. J.; Wolverton, C.; Kanatzidis, M. G. *Science* **2015**, *351* (6269), 141–144.
266. Huang, L.; Lu, J.; Ma, D.; Ma, C.; Zhang, B.; Wang, H.; Wang, G.; Gregory, D. H.; Zhou, X.; Han, G. *J. Mater. Chem. A* **2020**, *8*, 1394–1402.
267. Duong, A. T.; Nguyen, V. Q.; Duvjir, G.; Duong, V. T.; Kwon, S.; Song, J. Y.; Lee, J. K.; Lee, J. E.; Park, S.-D.; Min, T.; Lee, J.; Kim, J.; Cho, S. *Nat. Commun.* **2016**, *7*, 13713.
268. Liu, Y.; Calcabrini, M.; Yu, Y.; Lee, S.; Chang, C.; David, J.; Ghosh, T.; Spadaro, M. C.; Xie, C.; Cojocaru-Mirédin, O.; Arbiol, J.; Ibáñez, M. *ACS Nano* **2022**, *16* (1), 78–88.
269. Zhang, Q.; Liao, B.; Lan, Y.; Lukas, K.; Liu, W.; Esfarjani, K.; Opeil, C.; Broido, D.; Chen, G.; Ren, Z. *Proc. Natl. Acad. Sci.* **2013a**, *110* (33), 13261–13266.
270. Ju, H.; Kim, J. *Chem. Eng. J.* **2020**, *402*, 126274.
271. Zhao, H.; Xu, X.; Li, C.; Tian, R.; Zhang, R.; Huang, R.; Lyu, Y.; Li, D.; Hu, X.; Pan, L.; Wang, Y. *J. Mater. Chem. A* **2017**, *5*, 23267–23275.
272. Lohani, K.; Nautiyal, H.; Ataollahi, N.; Anselmi-Tamburini, U.; Fanciulli, C.; Scardi, P. *ACS Appl. Nano Mater.* **2023**, *6* (7), 6323–6333.
273. Shi, X.; Xi, L.; Fan, J.; Zhang, W.; Chen, L. *Chem. Mater.* **2010**, *22* (22), 6029–6031.
274. Marcano, G.; Rincon, C.; de Chalbaud, L. M.; Bracho, D. B.; Perez, G. S. *J. Appl. Phys.* **2001**, *90*, 1847.
275. Zhai, Y.-T.; Chen, S.; Yang, J.-H.; Xiang, H.-J.; Gong, X.-G.; Walsh, A.; Kang, J.; Wei, S.-H. *Phys. Rev. B: Condens. Matter Mater. Phys.* **2011a**, *84*, 075213.
276. Zhang, A.; Chen, Q.; Yao, W.; Yang, D.; Wang, G.; Zhou, X. *J. Electron. Mater.* **2016**, *45*, 1935.
277. Liu, M. L.; Huang, F. Q.; Chen, L. D.; Chen, I. W. *Appl. Phys. Lett.* **2009**, *94*, 202103.
278. Sarkar, S.; Das, B.; Midya, P. R.; Das, G. C.; Chattopadhyay, K. K. *Mater. Lett.* **2015**, *152*, 155–158.

279. Shan, Y.; Li, Y.; Pang, H. *Adv. Funct. Mater.* **2020**, *30* (23), 2001298.
280. Brousse, T.; Lee, S. M.; Pasquereau, L.; Defives, D.; Schleich, D. M. *Solid State Ionics* **1998**, *113–115*, 51–56.
281. Li, S.; Zheng, J.; Hu, Z.; Zuo, S.; Wu, Z.; Yan, P.; Pan, F. *RSC Adv.* **2015**, *5*, 72857–72862.
282. Zhai, C.; Du, N.; Yang, H. Z. D. *Chem. Commun.* **2011b**, *47*, 1270–1272.
283. Choi, J.; Jin, J.; Jung, I. G.; Kim, J. M.; Kim, H. J.; Son, S. U. *Chem. Commun.* **2011**, *47*, 5241–5243.
284. Davitt, F.; Stokes, K.; Collins, T. W.; Roldan-Gutierrez, M.; Robinson, F.; Geaney, H.; Biswas, S.; Chang, S. L. Y.; Ryan, K. M.; Reid, G.; Holmes, J. D. *ACS Appl. Energy Mater.* **2020**, *3* (7), 6602–6610.
285. Kravchyk, K.; Protesescu, L.; Bodnarchuk, M. I.; Krumeich, F.; Yarema, M.; Walter, M.; Guntlin, C.; Kovalenko, M. V. *J. Am. Chem. Soc.* **2013**, *135* (11), 4199.
286. Wu, C.; Hu, Z.; Wang, C.; Sheng, H.; Yang, J.; Xie, Y. *Appl. Phys. Lett.* **2007**, *91*, 143104.
287. Qu, B.; Zhang, M.; Lei, D.; Zeng, Y.; Chen, Y.; Chen, L.; Li, Q.; Wang, Y.; Wang, T. *Nanoscale* **2011a**, *3*, 3646–3651.
288. Zhang, Z.; Fu, Y.; Zhou, C.; Li, J.; Lai, Y. *Solid State Ionics* **2015**, *269*, 62–66.
289. Zhang, Z.; Zhou, C.; Jia, M.; Fu, Y.; Li, J.; Lai, Y. *Electrochim. Acta* **2014c**, *143*, 305–311.
290. Tao, H.-C.; Zhu, S.-C.; Yang, X.-L.; Zhang, L.-L.; Ni, S.-B. *J. Electroanal. Chem.* **2016**, *760*, 127.
291. Qu, B.; Li, H.; Zhang, M.; Mei, L.; Chen, L.; Wang, Y.; Li, Q.; Wang, T. *Nanoscale* **2011b**, *3*, 4389.
292. Jiang, Q.; Chen, X.; Gao, H.; Feng, C.; Guo, Z. *Electrochim. Acta* **2016**, *190*, 703.
293. Inamdar, A. I.; Hou, B.; Chavan, H. S.; Salunke, A. S.; Han, J.; Shin, G.; Park, S.; Yeon, S.; Shrestha, N. K.; I, H.; Kim, H. *Dalton Trans.* **2022**, *51*, 14535–14544.
294. Setayeshmehr, M.; Haghighi, M.; Mirabbaszadeh, K. *Energy Storage* **2022**, *4* (4), e295.
295. Wang, H.; Chao, D. L.; Liu, J.; Lin, J.; Shen, Z. X. *2D Mater.* **2018**, *5* (3), 031005.
296. Isacfranklin, M.; Yuvakkumar, R.; Ravi, G.; Hong, S. I.; Shini, F.; Thambidurai, M.; Dang, C.; Velauthapillai, D. *Sci. Rep.* **2020**, *10*, 19198.
297. Isacfranklin, M.; Yuvakkumar, R.; Ravi, G.; Velauthapillai, D.; Pannipara, M.; Al-Sehemi, A. G. *Nanoscale Adv.* **2021b**, *3*, 486–498.
298. Ou, J. Z.; Ge, W.; Carey, B.; Daeneke, T.; Rotbart, A.; Shan, W.; Wang, Y.; Fu, Z.; Chrimes, A. F.; Wlodarski, W.; Russo, S. P.; Li, Y. X.; Kalantar-Zadeh, K. *ACS Nano* **2015**, *9* (10), 10313.
299. Yan, W.-J.; Chen, D.-Y.; Fuh, H.-R.; Li, Y.-L.; Zhang, D.; Liu, H.; Wu, G.; Zhang, L.; Ren, X.; Cho, J.; Choi, M.; Chun, B. S.; Coileain, C. O.; Xu, H.-J.; Wang, Z.; Jiang, Z.; Chang, C.-R.; Wu, H.-C. *RSC Adv.* **2019**, *9*, 626–635.
300. Sucharitakul, S.; Kumar, U. R.; Sankar, R.; Chou, F.-C.; Chen, Y.-T.; Wang, C.; He, C.; He, R.; Gao, X. P. A. *Nanoscale* **2016**, *8*, 19050–19057.
301. Afsar, M. F.; Rafiq, M. A.; Tok, A. I. Y. *RSC Adv.* **2017**, *7*, 21556–21566.